



# 1 Assessment of Disdrometer Data Quality Control Methods for 2 Precipitation Measurements Based on Wet-Bulb Temperature

3 Hyeon-Joon Kim<sup>1</sup>, Sung-Ho Suh<sup>2</sup>, Jongyun Byun<sup>3</sup>, Changhyun Jun<sup>4</sup>

4 <sup>1</sup>Center of Oceanic and Meteorological Information, Pukyong National University, Busan, South Korea

5 <sup>2</sup>Flight Safety Technology Division, NARO Space Center, Korea Aerospace Research Institute, Goheung, South Korea

6 <sup>3</sup>Department of Civil, Environmental and Architectural Engineering, Korea University, Seoul, South Korea

7 <sup>4</sup>School of Civil, Environmental and Architectural Engineering, Korea University, Seoul, South Korea

8

9 Correspondence to: Changhyun Jun (cjun@korea.ac.kr)

10 **Abstract.** This study focuses on the reliability assessment of precipitation data calculated from drop size distribution (DSD)  
11 based on disdrometer data observations according to wet-bulb temperature ( $T_w$ ). Three distinct quality control (QC) methods  
12 based on fall velocity were implemented and validated against measurements from tipping-buckets and weighing rain gauges  
13 collected from January 2020 to February 2024. The analysis indicated that all QC methods exhibited high reliability  
14 (correlation coefficient (CC) > 0.98) for rainfall conditions when  $T_w$  was above 5 °C, with a mean absolute percentage error  
15 (MAPE) of approximately 8.5%. However, the precision of precipitation measurements exhibited a notable decline when  $T_w$   
16 was below 2 °C, as indicated by a CC of less than 0.6 and MAPE exceeding 30%. This reduction in accuracy can primarily  
17 be attributed to the outcomes of the QC methods, which rely on the falling velocity, given that raindrops and solid particles  
18 were observed within the specified  $T_w$  range. When considering the melting of snow particles at  $T_w$  ranging from 0 °C to 2 °C,  
19 the CC approached 0.9, suggesting enhanced measurement reliability. The findings of this study indicate that  $T_w$  is a more  
20 effective variable than air temperature ( $T_{air}$ ) for differentiating the precipitation types. This conclusion arises from the  
21 observation that the fall velocity of hydrometeors does not reach the terminal velocity of raindrops, even within the  $T_{air}$  range  
22 of 1–5 °C, coupled with the broad distribution of fall velocities. The DSD shape demonstrated stability across multiple QC  
23 methods when  $T_w$  was equal to or greater than 2 °C. In contrast, considerable variations were observed at lower temperatures,  
24 where particles with diameters ranging from 1 to 2 mm exhibited irregular distribution patterns at temperatures below 1 °C.  
25 These results suggest that DSD parameters should be derived from disdrometer data obtained under conditions where  $T_w$  is  
26 above 2 °C to ensure the reliability of the findings. This study provides critical insights for improving precipitation  
27 measurement techniques and DSD analyses in regions with variable temperature conditions.



## 28 **1 Introduction**

29 Several factors influence the variability in precipitation development, including atmospheric water vapor content, vertical  
30 airflow intensity, and temperature and humidity distributions in the vertical profile (Lintner et al., 2017; Padullés et al.,  
31 2022). These factors can be categorized as climatological, geographical, or topographical. Climatological factors include  
32 alterations in atmospheric water vapor resulting from long-term temperature changes, developmental shifts associated with  
33 temperature variations in the upper and lower atmospheric layers, and thermodynamic effects linked to changes in land cover  
34 based on climatic characteristics (Dahlström, 2021; Lu et al., 2024). Geographical and topographical factors include the  
35 convergence of water vapor due to mountainous terrain, which facilitates vertical precipitation development (Insel et al.,  
36 2010; Lee et al., 2014; Kim et al., 2019), and the generation of vertical flow resulting from increased friction at low levels  
37 due to coastal topography (Du and Chen, 2019; Yao et al., 2021). Additionally, precipitation development can be influenced  
38 by the temperature differential between the sea and air, particularly when cold air from inland regions moves over water  
39 bodies during winter (Steenhugh, 2020). Various environmental factors can influence the disparities in warm precipitation  
40 processes, such as collision-coalescence, evaporation, and accretion, which are contingent upon the vertical development of  
41 precipitation types, including stratiform, convective, and typhoon-related precipitation. Similarly, cold precipitation  
42 processes such as snow riming, melting, and ice crystal growth are affected by these environmental variables. These factors  
43 contribute to the development of diverse hydrometeors including rain, snow, and graupel, which are influenced by  
44 temperature variations (Mahes Kumar et al., 2018; Yi et al., 2021). The differences in the precipitation development processes  
45 ultimately lead to variations in the total precipitation observed at the surface. Therefore, it is crucial to acquire data that  
46 accurately reflects the microphysical characteristics of precipitation to enhance precipitation monitoring. Furthermore,  
47 analyses based on long-term observational data are essential to identify the universal characteristics that account for the  
48 temporal variability of precipitation.

49 The utilization of long-term observational data considerably reduces errors, mainly by rectifying inaccuracies in the  
50 observational data and eliminating outliers. Even among instruments that measure the same meteorological parameters, the  
51 threshold values for outlier removal may vary based on the installation conditions and surrounding environment.  
52 Additionally, biases in the observed values can arise owing to variations in the observation area and resolution, which are  
53 contingent on the type of instrument employed (Sypka, 2019; Segovia-Cardozo et al., 2021). Ground-based rain gauges can  
54 be categorized into two types based on their measurement method: tipping-buckets and weighing gauges. Although the  
55 tipping-bucket type demonstrates high accuracy in measuring rainfall, its efficacy in measuring snowfall during winter may  
56 be inferior to that of the weighing type because the observation value is recorded only when the precipitation in the bucket  
57 reaches a predetermined capacity (Savina et al., 2012; Kochendorfer et al., 2020). Comprehending the characteristics of  
58 observational instruments and the data they produce is imperative to ensure the reliability of the research findings derived  
59 from observational data.



60 The standard instruments used to observe precipitation include rain gauges and disdrometers. A rain gauge measures the total  
61 precipitation accumulated over a specified time interval. In contrast, a disdrometer assesses the size and concentration of  
62 precipitation particles, thereby enabling the determination of the precipitation intensity and type. The selection of an  
63 appropriate type of rain gauge is contingent on specific observational objectives such as monitoring heavy rain, light rain, or  
64 snow. Notable examples of disdrometers include the Particle Size and Velocity (PARSIVEL), Two-dimensional Video  
65 Disdrometer (2DVD), Joss-Waldvogel Disdrometer, and Precipitation Occurrence Sensor System. Disdrometers compute the  
66 size-specific concentration of particles, known as the Drop Size Distribution (DSD), by analyzing the variations in optical  
67 intensity as the particles traverse the observation zone of the sensor. In contrast to data obtained from rain gauges,  
68 disdrometer data offer a broader range of applications because they provide physical parameters, such as particle number  
69 concentration and fall velocity, and morphological characteristics, such as oblateness.

70 A typical application of disdrometer data involves formulating Quantitative Precipitation Estimation (QPE) equations, which  
71 are used in conjunction with remote sensing data such as radar observations. To derive rainfall information from remote  
72 sensing data, researchers can leverage the correlation between rain rate and radar reflectivity values, an observational  
73 variable in remote sensing, to measure variations in rainfall (Ji et al., 2019; Tang et al., 2024). Additionally, DSD  
74 information obtained from disdrometer observations is instrumental in parameterizing microphysical schemes within  
75 numerical weather prediction models (Yang et al., 2019; Iversen et al., 2021). Microphysical schemes can be categorized  
76 into bin and bulk types (Hu and Igel, 2023). The bin scheme accurately simulates the distributional differences between  
77 hydrometeor types by accounting for their size-dependent number concentration. However, this approach is limited by its  
78 high computational demand and the need for substantial hardware resources during the simulation process. Consequently,  
79 bulk schemes are predominantly employed in weather prediction models. This approach simulates microphysical processes  
80 based on the relationships between particle diameter and concentration distributions for various hydrometeor types. The  
81 DSD model considerably influences the quantitative differences in the estimated precipitation property outcomes. As the  
82 reliability of the DSD model improves, so does the accuracy of the precipitation simulation and forecasting.

83 The DSD model used in the QPE and microphysical schemes of remote sensing encompasses various models, such as the  
84 Marshall-Palmer, exponential (Marshall and Palmer, 1948), and gamma models (Ulbrich, 1983). The configuration of each  
85 model is contingent on the specific parameters being analyzed, with the shape and slope variables in the DSD model varying  
86 according to the concentration distribution based on the particle diameter (Smith, 2003; Liu et al., 2021). The DSD is  
87 affected by several factors, such as the type of rainfall (Deo and Walsh, 2016), intensity of rainfall (Thomas et al., 2021), and  
88 climatological and topographical characteristics of the region where precipitation occurs and develops (Kim et al., 2022).  
89 Consequently, it is imperative to acquire DSD model parameters and reflectivity data by collecting highly reliable  
90 observational data that accurately represent precipitation characteristics to enhance the precision of rainfall estimations and  
91 simulations based on DSD. Furthermore, disdrometer data can be used to estimate rainfall erosivity (Serio et al., 2019).  
92 Enhancing the accuracy of rainfall erosivity estimates can facilitate the assessment of the impact of rainfall on soil erosion  
93 and serve as a foundation for developing countermeasures through spatial analysis and monitoring of soil erosion risk areas



94 using remote sensing data. Reliable precipitation observational data for estimating rainfall erosivity can aid in analyzing the  
95 effects of erosion resulting from alterations in rainfall patterns due to climate change.

96 Various quality control (QC) methods for disdrometer data have been suggested to enhance the accuracy of derived  
97 measurements (Kruger and Krajewski, 2002; Jaffrain and Berne, 2011; Raupach et al., 2015). QC approaches for  
98 disdrometer data primarily rely on the falling velocity of raindrops. In the absence of a substantial wind influence or particle  
99 collisions during descent, the fall velocity of a raindrop tends to increase with its diameter, ultimately reaching a terminal  
100 velocity. Terminal velocity is achieved when the forces of air resistance and gravitational pull are in equilibrium, resulting in  
101 no further particle acceleration. Studies have been conducted to determine the terminal velocities of raindrop particles (Atlas  
102 et al., 1973; Beard, 1977; Brandes et al., 2002), which have led to the development of QC methods that use terminal velocity  
103 measurements. Kruger and Krajewski (2002) elucidated the structural design and operational principles of a 2DVD system,  
104 and noted that the recorded data indicated a fall velocity of approximately  $400 \text{ m s}^{-1}$ . However, this value is not feasible for  
105 raindrops. To mitigate the impact of erroneous data (outliers) potentially arising from hardware malfunctions, inaccuracies in  
106 data processing, and environmental conditions at the observation site, we employed a comparative analysis of the empirical  
107 relationship of raindrops established by Atlas et al. (1973). Furthermore, recognizing that the disdrometer may either  
108 underestimate or overestimate the fall velocity of precipitation particles influenced by the horizontal movement due to wind,  
109 this study conducted QC by focusing exclusively on the vertical velocity measurements. Jaffrain and Berne (2011)  
110 conducted a study to address the uncertainties associated with sampling observations from PARSIVEL disdrometers. They  
111 argued that the collected precipitation data exhibit inherent variability and measurement errors attributable to the equipment  
112 used, necessitating the development of a method to mitigate these issues and enhance data reliability. The authors proposed a  
113 method for eliminating anomalous data, such as outliers (values that are not physically plausible), instances of particle  
114 splashing (where the same particle is detected multiple times), and non-meteorological data. This preprocessing approach  
115 effectively diminished the sampling uncertainty of various parameters, including rain rate.

116 Raupach et al. (2015) conducted a study using data from the PARSIVEL and 2DVD to establish a correction factor for  
117 number concentration based on observations from the PARSIVEL disdrometer. The authors noted a tendency for  
118 PARSIVEL to overestimate the number of small droplets measuring between 0.2 and 0.4 mm and larger particles measuring  
119 2.4 mm or more. Furthermore, the measured fall velocity of larger droplets was lower than the actual terminal velocity.  
120 Anomalous data can lead to DSD distortions, which can compromise the accuracy of precipitation measurements and radar-  
121 based rainfall estimates. The focus of these studies was primarily on rainfall particles and it was determined that the  
122 quantitative accuracy of rainfall estimates improved when the aforementioned QC methods were applied across various  
123 environmental conditions.

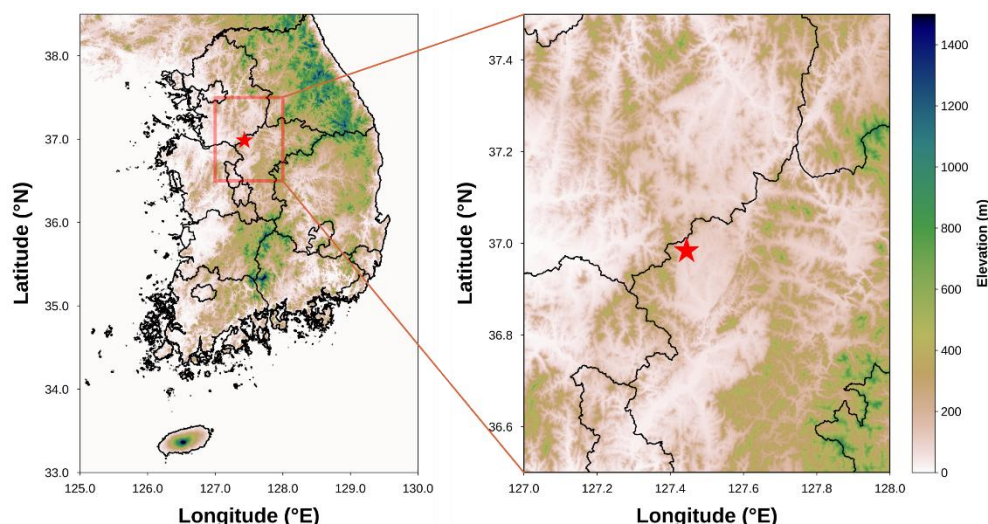
124 Snow particles exhibit a variety of forms such as needles, dendrites, and granules, which are influenced by temperature and  
125 humidity. These variations in shape arise from the specific conditions under which the particles form and develop, leading to  
126 differences in their densities and fall velocities (Barthazy and Schefold, 2006; Vázquez-Martín et al., 2021). Furthermore,  
127 snow particles are more susceptible to wind because of their lower density and larger surface area than raindrops.



128 Consequently, fall-velocity-based QC methods for eliminating non-meteorological particles (such as leaves, dust, and insects)  
129 are limited in their effectiveness because they primarily target solid particles with low fall velocities. Given the diverse  
130 shapes and fall speeds of snow particles, the mixing of raindrops and snow during precipitation events may lead to an  
131 underestimation of errors when applying conventional disdrometer QC methods. Therefore, it is imperative to establish  
132 objective criteria for differentiating rainfall and snowfall conditions to enhance the accuracy of rainfall analysis using  
133 disdrometer data. Ding et al. (2014) emphasized the significance of accurately classifying precipitation types for surface  
134 energy balance and hydrological process research. They aimed to develop a method for identifying precipitation types by  
135 analyzing 30 years of observational data. Their investigation focused on the correlation between precipitation type and  
136 various meteorological variables, including wet-bulb temperature ( $T_w$ ), relative humidity ( $RH$ ), and surface elevation. These  
137 findings indicate that using  $T_w$  as a reference variable for determining precipitation type is more reliable than relying on air  
138 temperature ( $T_{air}$ ). Furthermore, the proposed model, which incorporated  $T_w$ , demonstrated a determination accuracy  
139 exceeding 88%.  
140 This study aims to evaluate the quantitative accuracy of rainfall measurements obtained from a disdrometer in relation to  
141 varying  $T_w$  conditions. Furthermore, this study seeks to establish environmental criteria to ensure the reliability of the  
142 parameters used in the DSD model by using long-term rainfall data collected through disdrometer observations. A  
143 comparative analysis of the disdrometer data was performed using different QC methods to examine the discrepancies  
144 between these methods under varying  $T_w$  conditions.

## 145 **2 Data**

146 In this study, we evaluated the QC method applied to disdrometer data under varying precipitation conditions. To achieve  
147 this, we collected and analyzed regional observational data that accounted for the environmental factors associated with  
148 rainfall and snowfall. This study used data from a 2DVD installed at an observatory (Fig. 1) operated by the Weather Radar  
149 Center of the Korea Meteorological Administration. The integrity of the 2DVD data was corroborated through comparisons  
150 with measurements obtained from the tipping-bucket and weighing rain gauges. The analysis included observational data  
151 collected between January 2020 and February 2024.



152 **Figure 1: Location of ground observation station.**

## 153 2.1 Disdrometer

154 The 2DVD (Kruger and Krajewski, 2002) used for the validity analysis of the disdrometer was an optical disdrometer  
155 developed by Joanneum Research. This instrument operates by projecting light through a bulb across a designated  
156 observation area and capturing the intensity of the transmitted light using a camera positioned on the opposite side (Fig. 2).  
157 When a particle, such as a raindrop, traverses the observation area (10 cm<sup>2</sup>) illuminated by the light sheet, its diameter is  
158 determined by analyzing the reduction in the intensity and width of the light during its passage. Furthermore, the system  
159 employs two cameras to observe the particles from orthogonal angles, allowing the fall velocity to be calculated based on the  
160 differential height of the light sheet in the two orientations and time taken for the particles to descend. The 2DVD's  
161 capability to acquire diameter and fall velocity data for individual particles offers superior temporal, dimensional, and  
162 velocity resolution compared to traditional disdrometer data, which typically provide channel-based information. The  
163 observational resolution of the camera was approximately 0.2 mm (512 pixels), making the particles smaller than the  
164 indistinguishable threshold (Grazioli et al., 2014). For quantitative validation using rain gauge data, the output time  
165 resolution was configured to one minute, with data classified at one-minute intervals.





166 **Figure 2: Two-dimensional video disdrometer.**

## 167 2.2 Rain gauge

168 Precipitation can occur in liquid droplets and solid particles, such as snow and graupel, when temperatures are at or near 0 °C.  
 169 To validate the disdrometer data under  $T_w$  conditions, an analysis was conducted using data from the tipping-bucket and  
 170 weighing-type rain gauges (Fig. 3). Each type of rain gauge offers an observational resolution of 0.1 mm and a temporal  
 171 resolution of 1 min. Both instruments were positioned within a 10 m radius of the 2DVD disdrometer.

(a) Tipping-bucket type



(b) Weighing type



172 **Figure 3: (a) Tipping-bucket rain gauge (0.1 mm) and (b) Weighing rain gauge (0.1 mm).**



### 173 3 Methods

174 Ding et al. (2014) argued that precipitation types such as rain, snow, and sleet co-occur when the  $T_{air}$  or  $T_w$  approaches or  
175 falls below 0 °C. They recommended using  $T_w$  as a more effective criterion for distinguishing between types of precipitation  
176 instead of relying solely on  $T_{air}$ . In this study, the temporal resolution of the temperature data differed from that of previous  
177 studies, which employed different temporal resolutions. To facilitate objective verification of the applicability of  $T_w$ ,  $T_{air}$  and  
178  $T_w$  were employed as criteria for classifying precipitation types, and a comprehensive analysis was conducted.

#### 179 3.1 Pre-processing of disdrometer data

180 A common QC approach for disdrometer data involves excluding non-meteorological data by analyzing fall velocity. In  
181 numerous studies, this QC process was implemented by establishing a threshold determined by the terminal velocity, as  
182 indicated in Eq. (1).

$$|V_{measured} - V_{ideal}| < C \times V_{ideal} \quad (1)$$

183 where  $V_{measured}$  and  $V_{ideal}$  represent the observed particle fall velocity (in m/s) and empirical fall velocity (or terminal  
184 velocity), respectively. Constant  $C$  denotes the setting constant, which indicates the percentage of the terminal velocity. The  
185 proportion of the removed particles may fluctuate based on the value of  $C$ . Numerous previous studies have provided  
186 validation results using various setting constants. Studies that employed 2DVD data (Kruger and Krajewski, 2002; Thurai  
187 and Bringi, 2005; Chang et al., 2009; Wen et al., 2018) predominantly adopted a setting constant of 0.4 (40%) during data  
188 processing. Studies that employed PARSIVEL data for analysis frequently applied a setting constant of 0.6, accounting for  
189 60% of the cases (Jaffrain and Berne, 2011; Friedrich et al., 2013; Ji et al., 2019; Kim et al., 2019). Given that previous  
190 studies have encompassed various precipitation types, such as heavy rainfall, typhoons, orographic rainfall, and  
191 thunderstorms, the established 40% and 60% QC conditions can be regarded as reliable preprocessing criteria for rainfall  
192 events.

193 Raupach and Berne (2015) used data from a 2DVD instrument to derive correction factors for the drop-diameter channel in  
194 the PARSIVEL dataset. The fall velocity filtering technique employed for the 2DVD and PARSIVEL data involved the  
195 exclusion of particles exhibiting a terminal velocity exceeding 4 m s<sup>-1</sup>, as shown in Eq. (2), those with a fall velocity below 3  
196 m s<sup>-1</sup>, as indicated in Eq. (3), and those larger than 7.5 mm, as shown in Eq. (4).

$$V_{measured} > V_{ideal} + 4 \quad (2)$$

$$V_{measured} > V_{ideal} - 3 \quad (3)$$

$$D > 7.5 \quad (4)$$

197 where  $D$  (in mm) is the diameter of the drop (or particle). This study involved a comparative analysis of the outcomes  
198 derived from the three QC methods based on fall velocity. Terminal velocity was determined using the equation established  
199 by Atlas et al. (1973) (Eq. (5)).

$$V(D) = 9.65 - 10.3 \exp(-0.6D) \quad (5)$$





Three QC methods were used to evaluate the research findings. Methods 1 and 2 are used for the  $\pm 40\%$  and  $\pm 60\%$  ranges of terminal velocity, respectively, whereas Method 3 is based on the approach proposed by Raupach and Berne (2015).

As the temperature decreased, various hydrometeors intermingled, resulting in a gradual reduction in the proportion of raindrops. Current QC methods are capable of eliminating low-density snow particles; however, to quantitatively compare and validate rainfall measurements obtained from rain gauge observations, particles that exhibit velocities below the threshold established for raindrops in each QC method are categorized as solid meteorological particles. In addition, analyses were conducted under the assumption that the solid particles melted and transformed into raindrops. This method aims to evaluate data from tipping-bucket rain gauges, which may exhibit diminished quantitative accuracy as the proportion of solid particles increases, and facilitate quantitative comparisons of rainfall observations derived from disdrometer data by implementing the QC method as the temperature decreases.

The equivalent-melted diameter ( $D_{eq}$ ) at which a snow particle can transition into a raindrop while preserving its mass was determined using Eq. (6), established by Delanoë et al. (2005). In this equation,  $\rho(D)$  ( $\text{g cm}^{-3}$ ) denotes the density of snow particles as a function of their diameter, while  $\rho_w$  ( $\text{g cm}^{-3}$ ) denotes the density of water. The density of the snow particles was computed based on the formula provided by Tiira et al. (2016) (Eq. (7)).

$$D_{eq} = \left( \rho(D) / \rho_w \right)^{1/3} D \quad (6)$$

$$\rho(D) = 0.226 D^{-1.004} \quad (7)$$

### 3.2 Raindrop size distribution

The 2DVD data can be configured to correspond to user-defined diameter bin sizes, which in turn influence the characteristics of the DSD output and the precision of the DSD model parameters (Marzuki et al., 2010). Consequently, this study aims to facilitate the analysis of PASIVEL and 2DVD data for comparative purposes. To achieve this, 2DVD data were processed using the diameter channel information derived from the PASIVEL data to compute the rain rate, number concentration, and DSD model parameters. Detailed information regarding the diameter and velocity channels of the PASIVEL data is provided in the appendices (Table A3-4). The rain rate ( $R$ ,  $\text{mm h}^{-1}$ ) is calculated using Eq. (8), which incorporates the number concentration and fall velocity for each diameter. In determining the DSD model parameters after the rain rate calculation, data from intervals where the rain rate was  $0.1 \text{ mm h}^{-1}$  or greater were considered, thereby minimizing the uncertainty associated with the DSD model. The gamma model, recognized for its reliability in representing DSD characteristics, was selected for analysis. This model (Eq. (9)) is characterized by the shape parameter  $\mu$  (Eq. (10)), slope parameter  $\Lambda$  ( $\text{mm}^{-1}$ ) (Eq. (11)), and intercept parameter  $N_0$  ( $\text{mm}^{-1} \text{m}^{-3}$ ) (Eq. (12)).

$$R = \frac{6\pi}{10^4} \int_{D_{min}}^{D_{max}} D^3 N(D) V(D) dD \quad (8)$$

$$N(D)_{\text{gamma}} = N_0 D^\mu \exp(-\Lambda D) \quad (9)$$



$$\mu = \frac{(7 - 11\eta) - [(7 - 11\eta)^2 - 4(\eta - 1)(30\eta - 12)]^2}{2(\eta - 1)} \quad (10)$$

$$\Lambda = \left[ \frac{M_2 \Gamma(\mu + 5)}{M_4 \Gamma(\mu + 3)} \right]^{1/2} = \left[ \frac{M_2(\mu + 4)(\mu + 3)}{M_4} \right]^{1/2} \quad (11)$$

$$N_0 = \frac{\Lambda^{(\mu+3)} M_2}{\Gamma(\mu + 3)} \quad (12)$$

226

227 The DSD parameters were derived from the  $n^{\text{th}}$  moment ( $M_n$ ), as indicated in Eq. (13), along with the  $\eta$  value, computed  
228 based on  $M_n$  as shown in Eq. (14).

$$M_n = \int_{D_{min}}^{D_{max}} D^n N(D) dD \quad (13)$$

$$\eta = \frac{\langle M_4 \rangle^2}{\langle M_2 \rangle \langle M_6 \rangle} = \frac{(\mu + 3)(\mu + 4)}{(\mu + 5)(\mu + 6)} \quad (14)$$

### 229 3.3 Wet-bulb temperature

230 Data from an Automatic Weather Station (AWS) installed at the observatory were used to compute the  $T_w$ . The  $T_{air}$  (in  
231 degrees Celsius) and  $RH$  (in percentages) values derived from the AWS observations were incorporated into the  $T_w$  (in  
232 degrees Celsius) calculation equation proposed by Stull (2011) (Eq. (15)) to determine the  $T_w$  value. The temporal resolution  
233 of  $RH$ ,  $T_{air}$ , and  $T_w$  was one minute, which was consistent with the temporal resolution of the disdrometer data.

$$T_w = T_{air} \text{atan}[0.151977(RH + 8.313659)^{1/2}] + \text{atan}(T_{air} + RH) - \text{atan}(RH - 1.676331) \quad (15)$$

$$+ 0.00391838(RH)^{\frac{3}{2}} \text{atan}(0.023101RH) - 4.686035$$

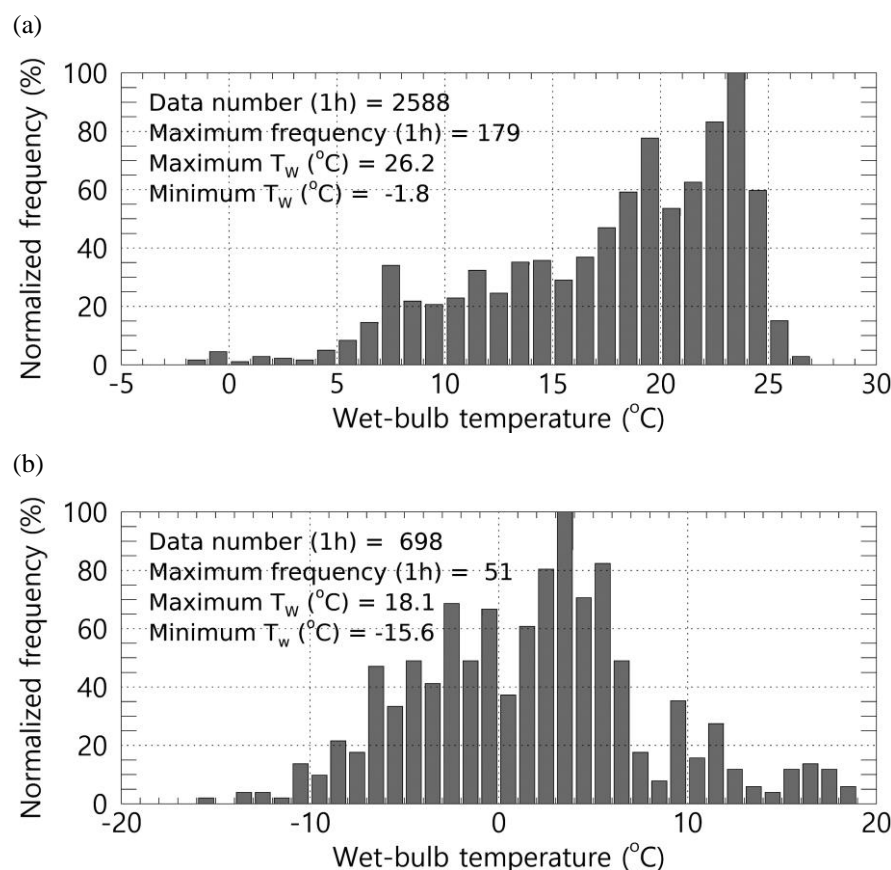
## 234 4 Results

### 235 4.1 Comparison of rainfall by the disdrometer pre-processing method

236 To validate the three QC methods employed for the disdrometer in this study, a comparative analysis was conducted between  
237 the rainfall measurements obtained from the disdrometer and those recorded by rain gauges. This comparison utilizes hourly  
238 accumulated rainfall data. Given that the QC methods for the disdrometer were specifically designed to address rainfall, the  
239 variable  $T_w$  was employed to differentiate between rainfall and snowfall, thereby facilitating the verification of rainfall  
240 timing. Ding et al. (2014) argued that snow is infrequently detected when  $T_w$  exceeds 5 °C. Figure 4 shows the distribution of  
241  $T_w$  during the analysis period, specifically for instances when the hourly average  $T_w$  was either above or below 5 °C. An  
242 examination of the one-minute  $T_w$  distribution during periods when the one-hour average  $T_w$  was 5 °C or higher (Fig. 4a)  
243 revealed a maximum  $T_w$  of 26.2 °C, with the highest proportion of values exceeding 20 °C. Conversely, the proportion of  
244 values falling below 5 °C was minimal, accounting for less than 5%. These findings suggest that it is feasible to delineate



245 rainfall periods using the hourly average  $T_w$  as a reference when comparing hourly accumulated rainfall values. In contrast,  
246 the distribution of one-minute  $T_w$  during hours when the average  $T_w$  was below 5 °C exhibited a broad range, with minimum  
247 and maximum  $T_w$  values exceeding 33 °C and a concentration of  $T_w$  values around 0 °C. This observation indicates notable  
248 variability in  $T_w$  under 5 °C or lower, suggesting that the observational area encompasses environmental conditions  
249 conducive to detecting diverse hydrometeors.



250 **Figure 4: Normalized frequency distribution of  $T_w$  during the analysis period (when the average hourly  $T_w$  is (a)  $T_w \geq 5$  °C, (b)  $T_w <$**   
251 **5 °C).**

252 Figure 5-6 presents a comparative analysis of hourly rainfall measurements obtained from the tipping-bucket and weighing  
253 rain gauge, specifically under conditions where the temperature ( $T_w$ ) equals or exceeds 5 °C, alongside data from the 2DVD  
254 observations. The results derived from the unprocessed raw data were analyzed to evaluate the impact of the QC procedures.  
255 The findings indicated a strong correlation, exceeding 0.98, between the 2DVD and rain gauge measurements, with a  
256 regression line slope of approximately unity. However, the raw data tended to overestimate the 2DVD-derived rainfall  
257 estimates compared to the QC-processed results. This discrepancy in the overestimation of the 2DVD data can be attributed  
258 to variations in the conditions under which particles are eliminated, which is contingent on the specific QC method  
259 employed. Following the application of the QC methods, the mean absolute percentage error (MAPE) demonstrated an



overall reduction compared with the raw data, suggesting that all QC methods possess quantitative reliability for rainfall data, with a maximum reduction of approximately 2.1%.

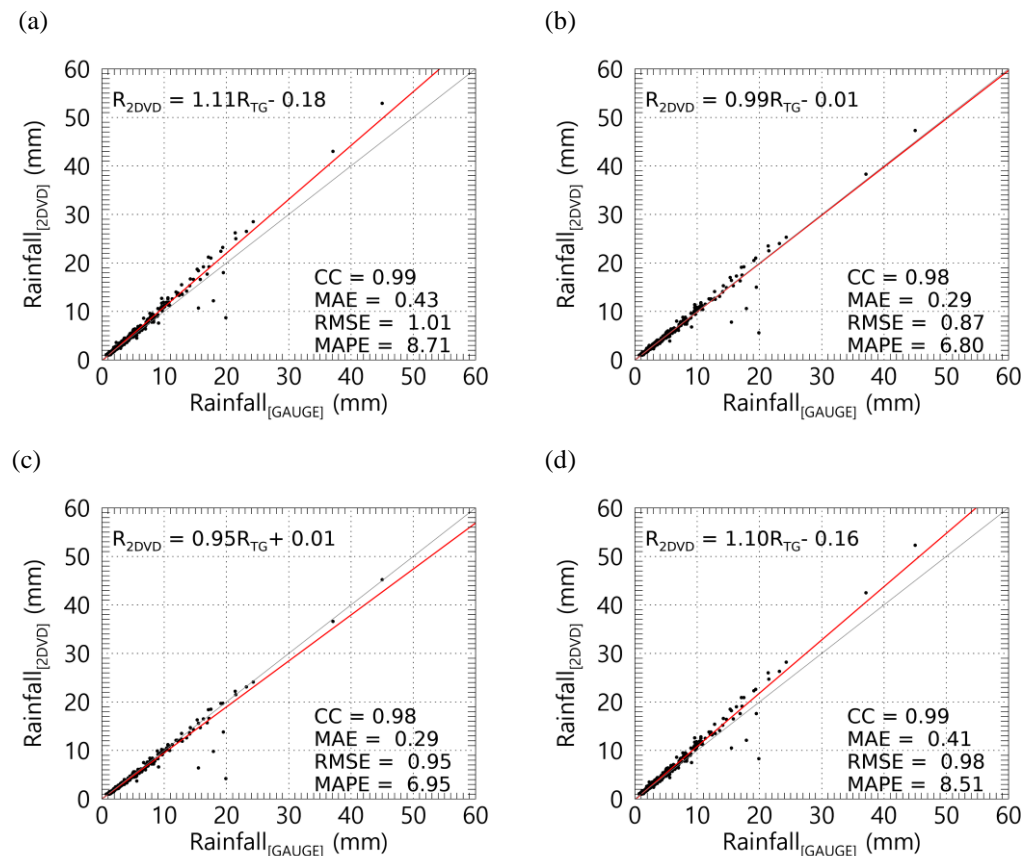


**Figure 5: Comparison of rainfall observed using the tipping-bucket rain gauge and 2DVD when  $T_w \geq 5$  °C ((a) Unfiltered, (b) Method 1, (c) Method 2, (d) Method 3).  $R_{2DVD}$  and  $R_{TG}$  denote the rainfall obtained from the 2DVD and a tipping-bucket rain gauge, respectively.**

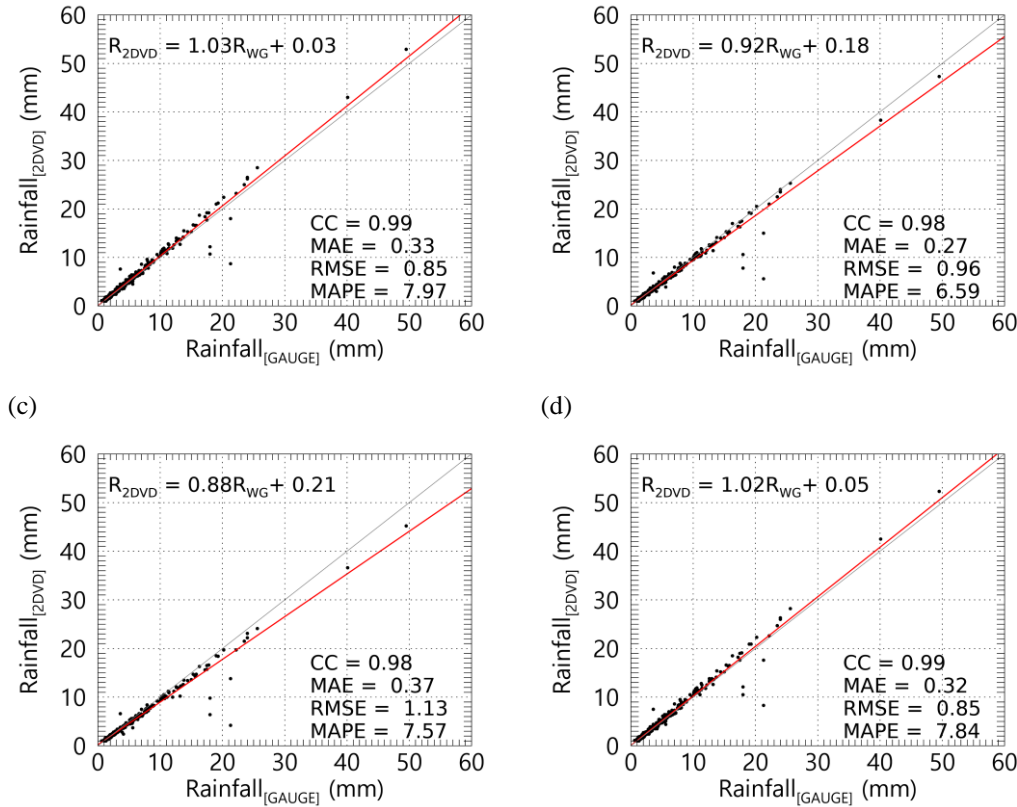


Figure 6: Comparison of rainfall observed using the weighing rain gauge and 2DVD when  $T_w \geq 5^\circ\text{C}$  ((a) Unfiltered, (b) Method 1, (c) Method 2, (d) Method 3).  $R_{WG}$  denotes the rainfall obtained from a weighing rain gauge.

## 4.2 Fall velocity of particle by temperature and wet-bulb temperature

### 4.2.1 Fall velocity distribution at $T_{air}$ and $T_w$

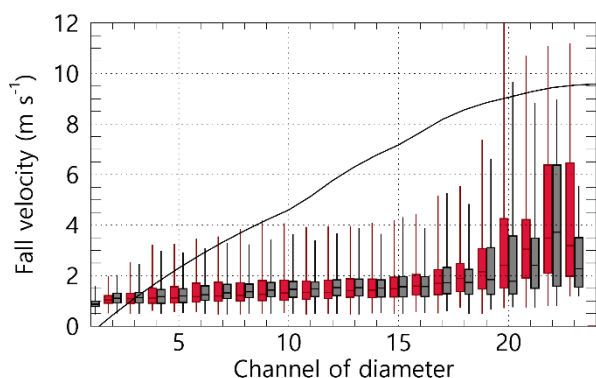
Figure 7 shows the distribution of the fall velocity with the diameter of precipitation particles (raindrops) under varying conditions of  $T_w$  and  $T_{air}$ . When the  $T_w$  and  $T_{air}$  ranged from  $-1$  to  $1^\circ\text{C}$ , the fall velocity distributions were relatively comparable. However, as the temperature exceeded  $0^\circ\text{C}$ , the fall velocity for CH 4 to 18 increased under  $T_w$  conditions, while the fall velocity for CH 19 to 23 increased under  $T_{air}$  conditions (Fig. 7(a-b)). Notably, when the temperature rose above  $1^\circ\text{C}$ , there was a notable increase in fall velocity; under  $T_w$  conditions, the distribution approached the terminal velocity of raindrops. Conversely, for diameters in the CH 12 or a higher range, the fall velocity remained at approximately  $5.5\text{ m s}^{-1}$  despite increases in diameter. Under  $T_{air}$  conditions, the fall velocity increased when temperatures were below  $1^\circ\text{C}$ . However, it remained lower than that observed under  $T_w$  conditions, with a broader distribution of fall velocities across the diameter channels (Fig. 7(c)). At  $2^\circ\text{C}$  or higher temperatures,  $T_w$  and  $T_{air}$  conditions yielded fall velocity distributions that were close to the terminal velocity of raindrops, with an increasing trend in distribution as temperature increased (Fig. 7(d-f)).



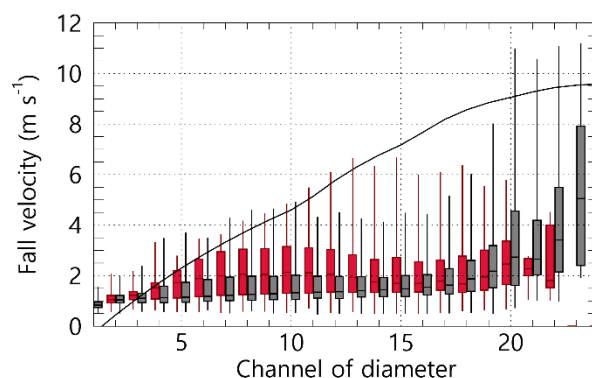


287 However, under  $T_{air}$  conditions, the fall velocity was notably low, remaining below  $2 \text{ m s}^{-1}$  for diameters of 3 mm (CH 17) or  
288 larger.

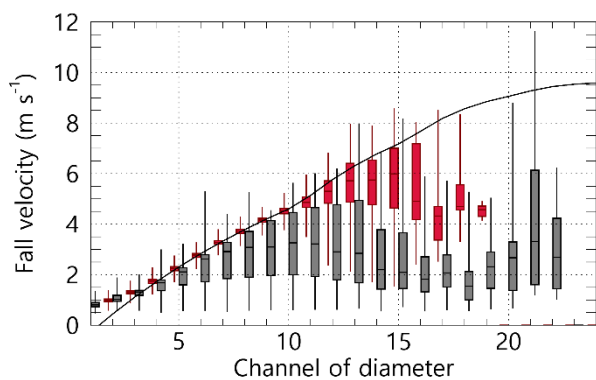
(a)  $-1^\circ\text{C} \leq T_w (T_{air}) < 0^\circ\text{C}$



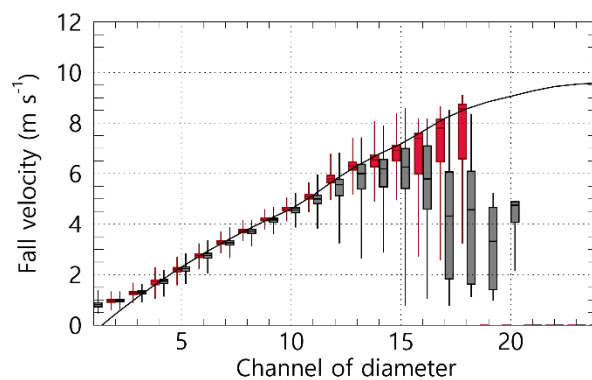
(b)  $0^\circ\text{C} \leq T_w (T_{air}) < 1^\circ\text{C}$



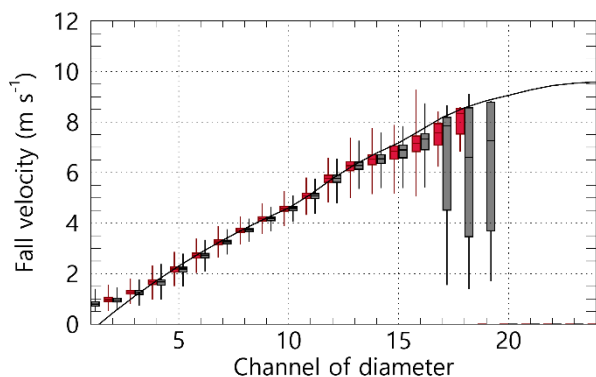
(c)  $1^\circ\text{C} \leq T_w (T_{air}) < 2^\circ\text{C}$



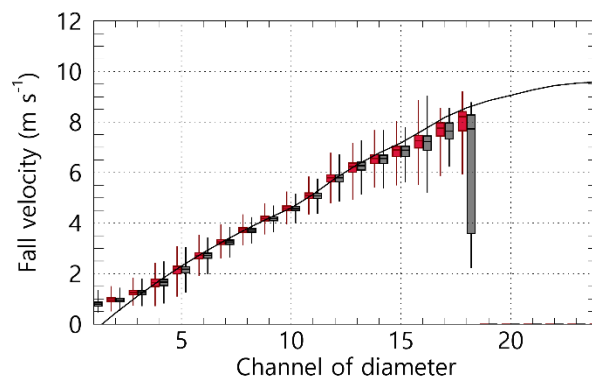
(d)  $2^\circ\text{C} \leq T_w (T_{air}) < 3^\circ\text{C}$



(e)  $3^\circ\text{C} \leq T_w (T_{air}) < 4^\circ\text{C}$



(f)  $4^\circ\text{C} \leq T_w (T_{air}) < 5^\circ\text{C}$



289 **Figure 7: Distribution of fall velocity by diameter channel based on  $T_w$  (red) and  $T_{air}$  (gray). The black solid line represents the**  
290 **terminal velocity of rain drops proposed by Atlas et al. (1973).**



Figure 8 shows the variability in fall velocity with respect to the changes in temperature. Notably, despite  $T_w$  and  $T_{air}$  exhibiting similar numerical ranges, the distribution of fall velocity was considerably broader under  $T_{air}$  conditions. When  $T_w$  exceeds 3 °C, the standard deviation across all diameter intervals remains low, approximately 1 m s<sup>-1</sup> or less. In instances where  $T_w$  ranges between 2 and 3 °C, an increase in distribution is observed for diameters of 2.5 mm or greater, while the standard deviation for diameters of 1 mm or more increases when  $T_w$  is between 1 and 2 °C. As temperature decreased, the range of diameters exhibiting increased fall velocity variability progressively expanded. According to the findings under  $T_{air}$  conditions, the standard deviation of fall velocity for diameters exceeding 1 mm begins to rise below 4 °C, with values surpassing 1 m s<sup>-1</sup> for diameters greater than 2 mm. The observation that when  $T_{air}$  is between 2 and 3 °C, the standard deviation of fall velocity for diameters ranging from 3 to 4 mm is considerably increased, exceeding 2 m s<sup>-1</sup> and reaching up to 4.5 m s<sup>-1</sup> is noteworthy. This broad fall velocity distribution suggests a mixture of various hydrometeors, complicating the differentiation between rain and snow based solely on fall velocity. Consequently, subsequent analyses were conducted using  $T_w$  as the criterion for distinguishing between rain and snow.

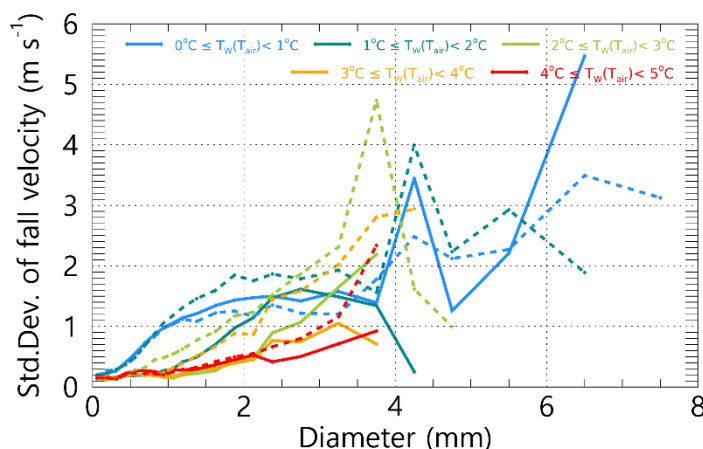


**Figure 8: Standard deviation of fall velocity by  $T_w$  (solid line) and  $T_{air}$  (dash line) range (1 °C interval).**

#### 4.2.2 Fall velocity distribution under rainfall condition

Figure 9 shows the distribution of fall velocities by diameter, derived from data collected when the  $T_w$  was at or above 5 °C. The central value of the fall velocity is consistent with the terminal velocity. This is within the range of fall velocities for raindrops, as established by the three different QC methods based on the fall velocity. It is important to note that precipitation particles (drops) may experience variations in their fall velocities owing to factors such as wind influence or collisions with obstacles during descent. The findings presented in Fig. 9 suggest that the observatory's measurements were not considerably affected by wind or obstacles, thereby confirming the reliability of the velocity observation data of the disdrometer.

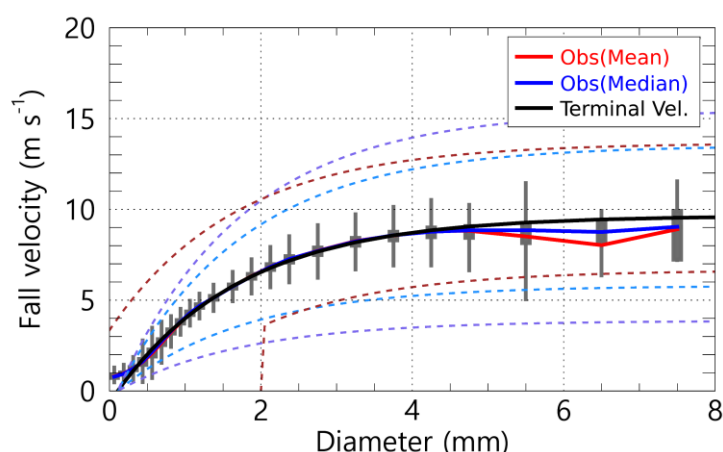


Figure 9: Distribution of fall speed by diameter under conditions of  $T_w \geq 5^\circ\text{C}$ , and effective fall velocity of raindrops by pre-processing methods (sky blue represents Method 1, purple Method 2, and brown Method 3).

An analysis of the fall velocity corresponding to temperature intervals ( $T_w$ ) of  $1^\circ\text{C}$  revealed that when  $T_w$  is at or above  $2^\circ\text{C}$ , the fall velocities correspond with those typically observed for raindrops. Conversely, at  $T_w$  values between  $1^\circ\text{C}$  and  $2^\circ\text{C}$ , particles with diameters of 2 mm or less fall within the raindrop velocity range; however, as the diameter increases to 2 mm or more, the fall velocity diminishes, stabilizing at approximately  $5\text{ m s}^{-1}$ . Temperature conditions ( $T_w$ ) may indicate a mixture of raindrops and snow particles. At temperatures below  $1^\circ\text{C}$ , the fall velocity of droplets with diameters of 4 mm or less decrease to approximately  $3\text{ m s}^{-1}$ , exhibiting a low-velocity distribution of  $5\text{ m s}^{-1}$  or less across all diameter ranges. This distribution suggests a higher proportion of solid (snow) particles when  $T_w$  is less than  $1^\circ\text{C}$ .

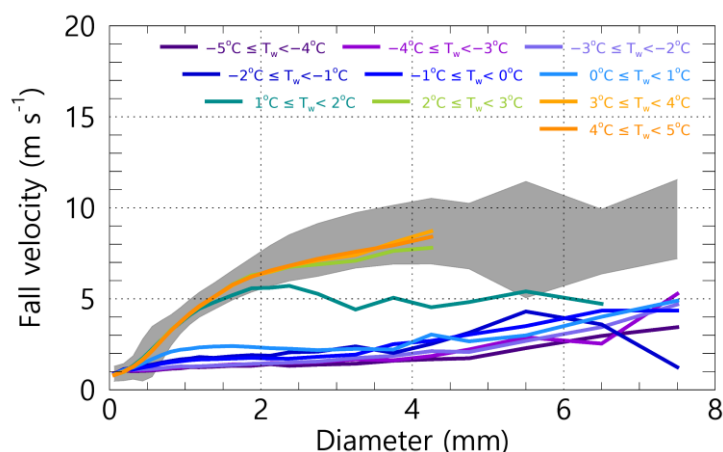


Figure 10: Distribution of fall velocity by diameter in each  $T_w$  range. The grey area in the figure represents the Q1 (25%) – Q3 (75%) for the fall velocity by diameter when  $T_w \geq 5^\circ\text{C}$ .



### 4.3 Accuracy of quantitative rainfall by wet-bulb temperature

Figures 11 and 12 show the outcomes of the comparative analysis and validation of rainfall measurements derived from the QC method applied to each  $T_w$  range, juxtaposed with the rainfall values obtained from a rain gauge. Figure 11 shows the results of applying the QC method, which effectively filtered out all particles except for raindrops. In contrast, Fig. 12 depicts the assumption that the particles exhibiting low fall velocities are snow that melts and transforms into raindrops. The verification metrics employed in this analysis included the Root Mean Square Error (RMSE), Mean Absolute Error (MAE), MAPE, Correlation Coefficient (CC), slope ( $a_1$ ), and intercept ( $a_0$ ) derived from Eq. (14), which is the first-order regression equation correlating rainfall measurements from the rain gauge and 2DVD.

$$R_{2DVD} = a_1 R_{Gauge} + a_0 \quad (14)$$

The  $a_1$  of the observed relationship indicates that when the  $T_w$  exceeds 2 °C, the value remains close to one before and following the application of QC. However, as  $T_w$  drops below 2 °C, the value of  $a_1$  either increases or decreases. A value of  $a_1$  greater than one suggests that the rainfall measurements derived from the 2DVD instrument tend to overestimate the corresponding values obtained from the rain gauge observations. In contrast, a value of less than one indicates an underestimation. Notably, in the absence of QC,  $a_1$  increases to two or more at temperatures below 0 °C, with the extent of overestimation intensifying as  $T_w$  decreases. This phenomenon is particularly evident when validated against a tipping-bucket rain gauge, where values of two or greater were recorded at temperatures ranging from 0 to 1 °C. This observation may be attributed to the different operational principles of the various rain gauge types within the specified  $T_w$  range (Fig. 11a). At  $T_w$  below 0 °C, the unfiltered data and Method 3 exhibit  $a_0$  values exceeding one, while Method 2 and Method 3 present  $a_1$  values below one. This discrepancy can be interpreted as a consequence of the varying quantities of preprocessed particles. For  $T_w$  values of 1 °C or higher,  $a_0$  is observed to range between 0 and 1; however, as  $T_w$  declines below 1 °C,  $a_0$  experiences a rapid increase. Method 3, which uses a smaller filter area for unfiltered particles and those with diameters of 2 mm or less, demonstrates  $a_0$  values of 0.2 or higher, exceeding those of Methods 1 and 2 (Fig. 11b).

The CC decreases substantially in the  $T_w$  range, whereas  $a_0$  increases considerably (Fig. 11f). The RMSE and MAE were recorded at low values of less than 0.3 mm and 0.2 mm, respectively, when  $T_w$  was at or above 2 °C; however, these errors increased as  $T_w$  decreased to 1 °C or lower, with the magnitude of errors following the order of Unfiltered, Method 3, Method 1, and Method 2, which corresponds to the increasing trend of  $a_1$ . In the range of 0 to 2 °C, the errors associated with results validated by the tipping-bucket rain gauge were greater than those from the weighing rain gauge (Fig. 11(c-d)). The MAPE exhibited its lowest error rate, below 20%, at temperatures between 3 and 4 °C. It progressively increased with a decrease in  $T_w$ , ultimately reaching values of approximately 30% or more at temperatures of 2 °C or lower.

Comparable findings were observed when it was assumed that the snow particles melted (Fig. 12), with an increase in error as the temperature ( $T_w$ ) dropped below 2 °C. The distinction between melted and unmelted snow particles was demonstrated using a weighing rain gauge as a verification tool. In scenarios where the melted state was disregarded at  $T_w$  values lower than 2 °C, the variability in the MAPE and CC was substantial, which was contingent upon fluctuations in  $T_w$ . Conversely,



355 the variability decreased when the melted state was considered, and the CC remained elevated approximately at 0.8 or above.  
356 The pronounced escalation in error within the 0–1 °C range can be attributed to precipitation detected by the 2DVD system  
357 that was not captured by the Tipping-bucket rain gauge (Fig. A1(f) in Appendix).  
358 Furthermore, the low volatility and high correlation observed in the verification results using the weighing rain gauge within  
359 the  $T_w$  range can be explained by incorporating raindrops and snow particles in the 0–1 °C range. By assuming melting of  
360 snow particles, both forms of precipitation can be integrated into precipitation calculations. The weighing rain gauge  
361 recorded precipitation values that accounted for the cumulative weight of all the raindrops and snow particles (Fig. A2(f) in  
362 the Appendix).

363  
364  
365  
366  
367  
368  
369  
370  
371  
372  
373  
374  
375  
376  
377  
378  
379  
380  
381  
382  
383  
384  
385  
386  
387



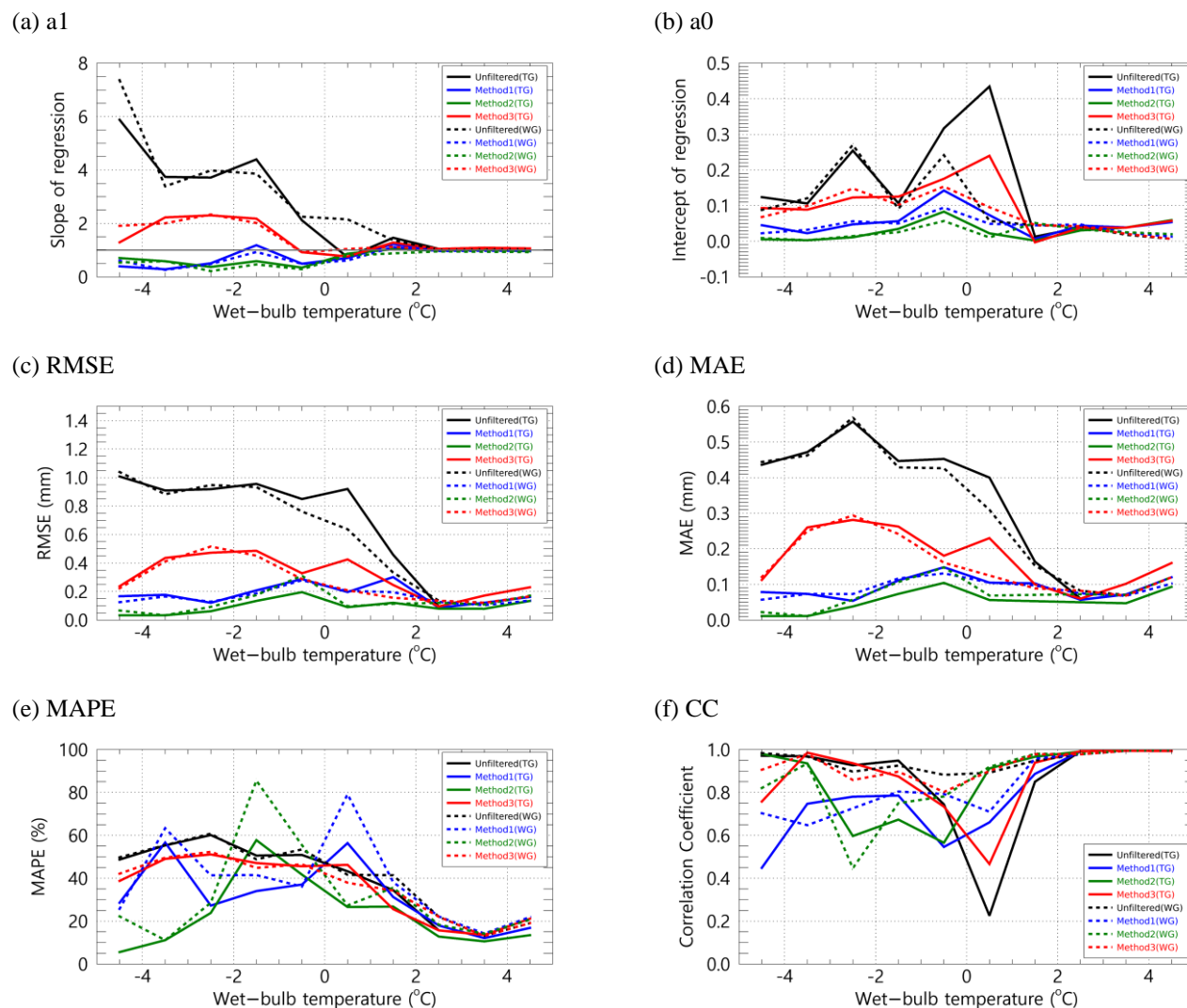


**Figure 11: Quantitative comparison of rainfall from a rain gauge (The solid line represents the tipping-bucket and the dash line represents the weighing rain gauge) and 2DVD by  $T_w$  (assuming that snow particles do not melt).**

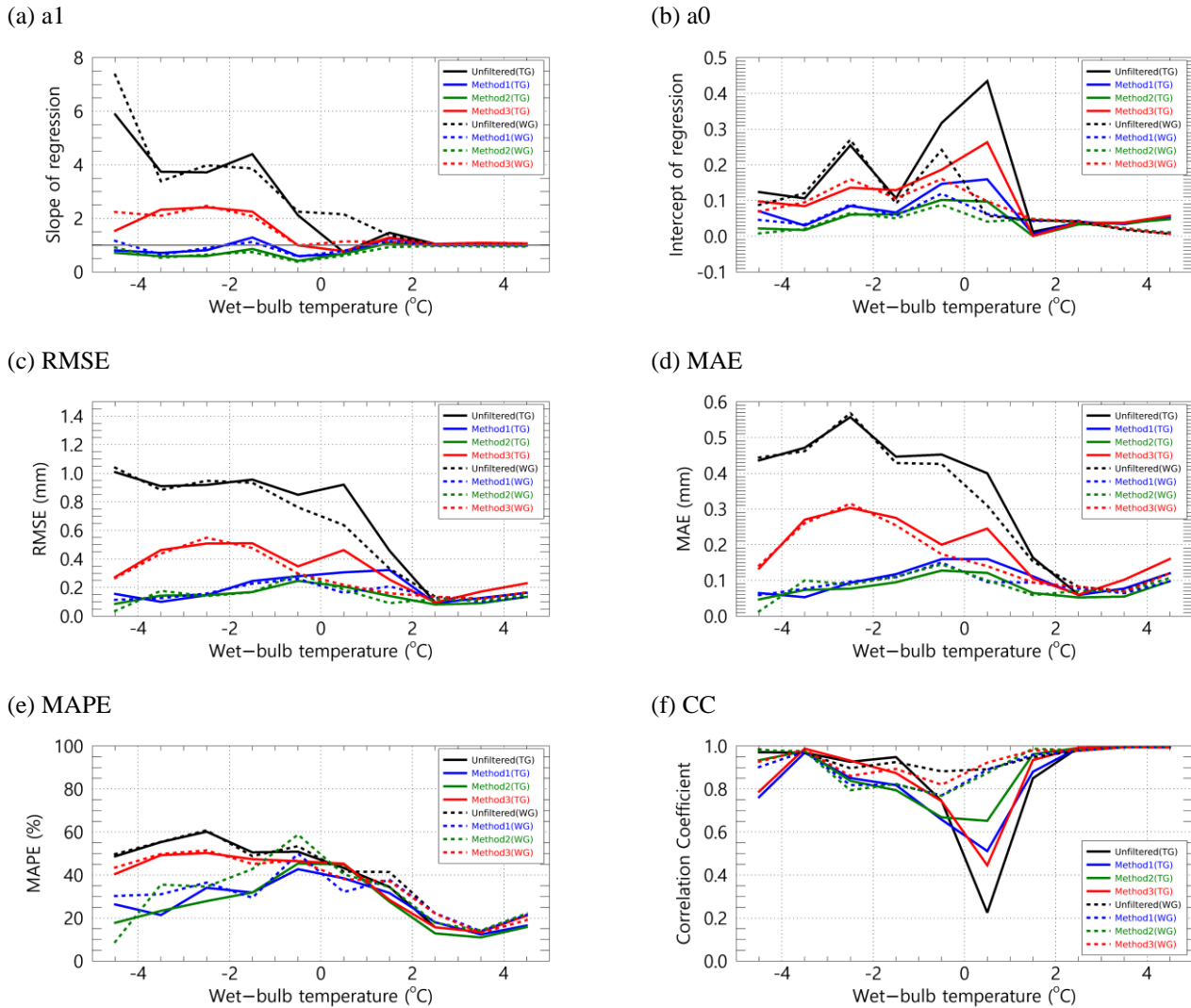


**Figure 12: Quantitative comparison of rainfall from a rain gauge (The solid line represents the tipping-bucket and the dash line represents the weighing rain gauge) and 2DVD by  $T_w$  (assuming that snow particles melt).**

#### 4.4 Particle filter rate

Precipitation measurements obtained from the disdrometer were derived from raindrop (or snow particle) accumulation. The quantitative errors associated with these precipitation measurements were assessed by comparing the removal rates of raindrops (or snow particles) using the QC method. Figure 13 shows the removal ratios corresponding to the  $T_w$  range and channel diameter. The two methods, Method 1 and Method 2, exhibit differences in the range of removal velocities based on particle diameter; specifically, Method 2 encompasses a broader spectrum of raindrop sizes compared to Method 1, leading to an increased removal rate when the  $T_w$  is below 0  $^{\circ}\text{C}$ . Notably, the removal rate for Method 2 surpasses that of Method 1 at temperatures lower than -2  $^{\circ}\text{C}$ . Conversely, Method 3 did not allow the removal of particles smaller than 2 mm (as

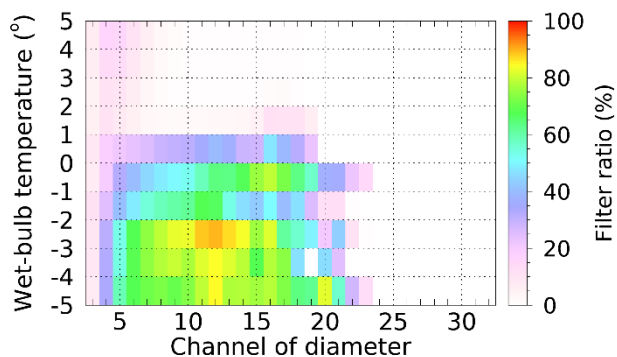


408 indicated in CH 14), regardless of their low fall velocity, resulting in a consistent removal rate of 0%, irrespective of  
409 variations in  $T_w$ . This suggests that the number of particles smaller than 2 mm may be greater in Methods 1 and 2.  
410 Furthermore, the removal rate was lower when snow particles were assumed to have melted than when they had not melted.  
411 Nonetheless, for particles with a diameter of 1 mm or less, the removal rate ranged from approximately 10% to 30% when  $T_w$   
412 exceeded 1 °C, which appears to be attributable to the removal of particles exhibiting a fall velocity that exceeds the  
413 raindrops.

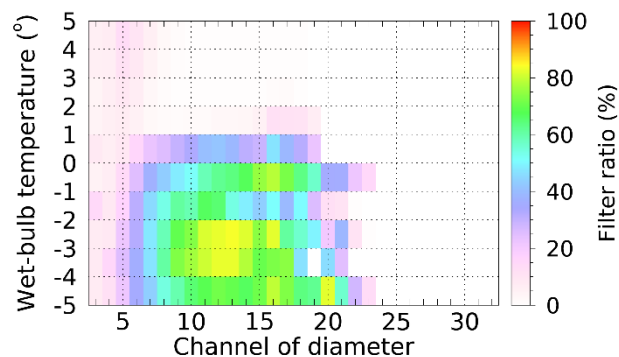
414  
415  
416  
417  
418  
419  
420  
421  
422  
423  
424  
425  
426  
427  
428  
429  
430  
431  
432  
433  
434  
435  
436  
437  
438  
439  
440  
441



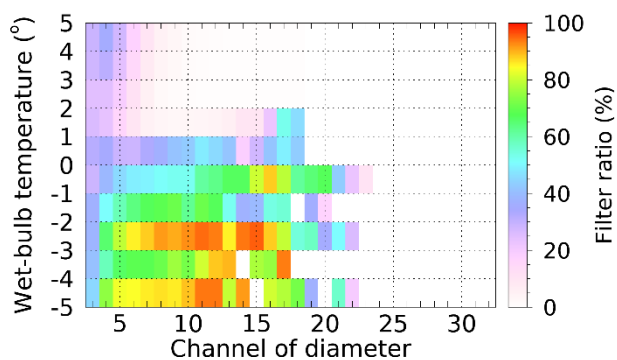
(a) Method 1



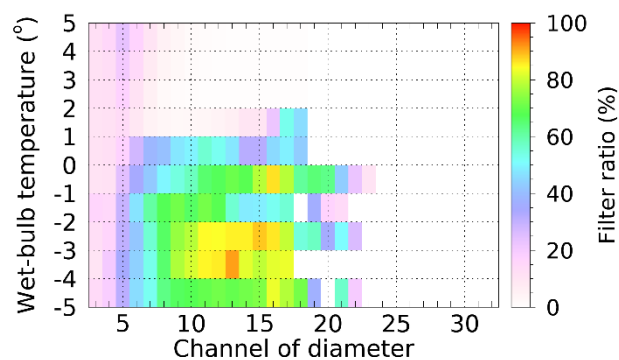
(b) Method 1 (melted)



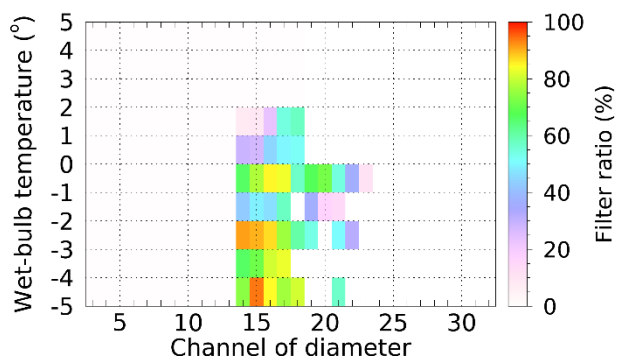
(c) Method 2



(d) Method 2 (melted)



(e) Method 3



(f) Method 3 (melted)

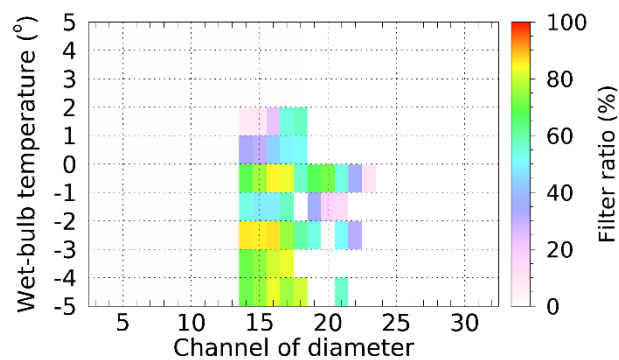


**Figure 13: Particle filter ratio by diameter channel for  $T_w$  according to the pre-processing method based on falling velocity.**



#### 447 4.5 Contribution rate by particle diameter to precipitation intensity

448 Figure 14 shows the contribution rate of the number concentration by diameter to the precipitation intensity as derived from  
449 the disdrometer data. It is observed that when the  $T_w$  exceeds 1 °C, the contribution rate remains approximately 20% or lower  
450 across all diameters. Conversely, when  $T_w$  is below 1 °C, the concentration of particles measuring 3 mm (CH 15) or larger  
451 considerably influences the calculation of precipitation intensity. The contribution rate of 1.25 to 1.75 mm diameter (CH 11  
452 to 13) decreased when the temperature was lower than 1 °C. The decrease in the contribution rate of drops smaller than 3  
453 mm and the increase in the contribution rate of larger drops was as a result of the decrease in the concentration of drops  
454 smaller than 3 mm through the QC process (Section 4.4), which increased the impact of relatively larger drops on the  
455 calculation of precipitation intensity. This phenomenon can be attributed to the direct proportionality of the precipitation  
456 intensity to  $N(D)$  and  $D^3$ , indicating that an increase in the particle diameter substantially affected the results. After QC, a  
457 substantial increase in the contribution rate for a specific diameter may affect the precipitation intensity owing to a decrease  
458 in the concentration of drops in the diameter range with a lower contribution rate.

459 In scenarios where it is assumed that snow particles have melted, the diameter of these particles decreases, increasing the  
460 concentration of smaller particles. As a result, the contribution rate of diameter from approximately 0.5 to 1 mm (CH 5 to 10)  
461 increased. Notably, in Method 3, there was a minimal removal of particles smaller than 2 mm, which resulted in negligible  
462 differences between the scenarios that accounted for the melted state of snow particles and those that did not.

463

464

465

466

467

468

469

470

471

472

473

474

475

476

477

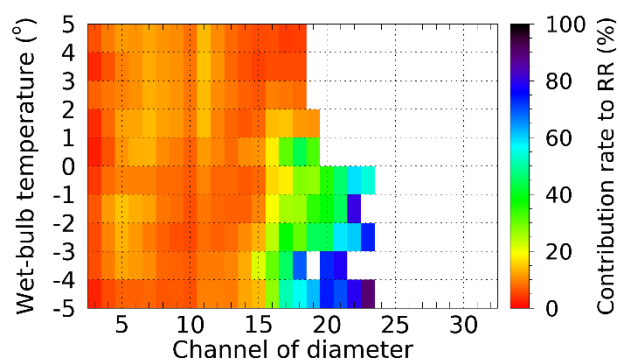
478

479

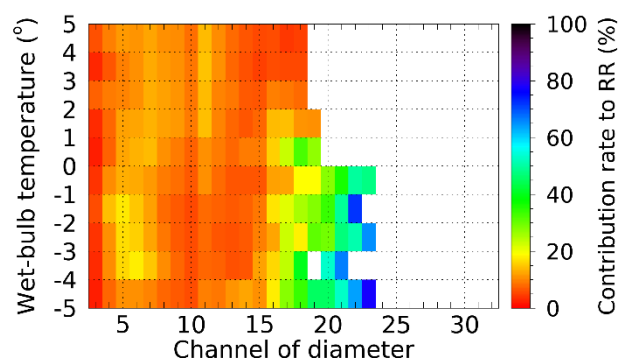




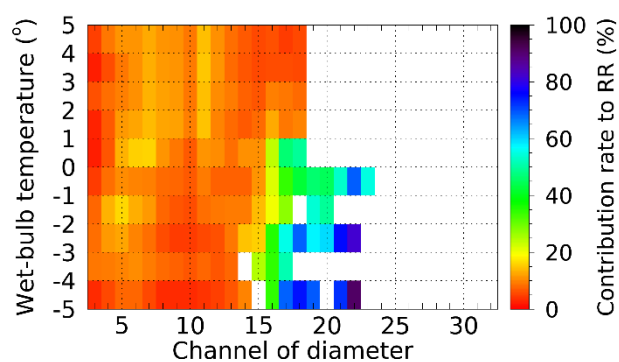
(a) Method 1



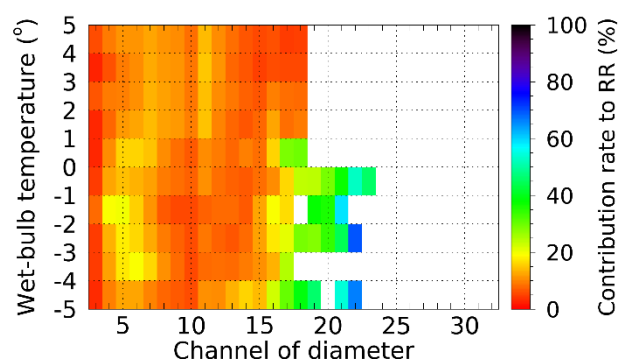
(b) Method 1 (melted)



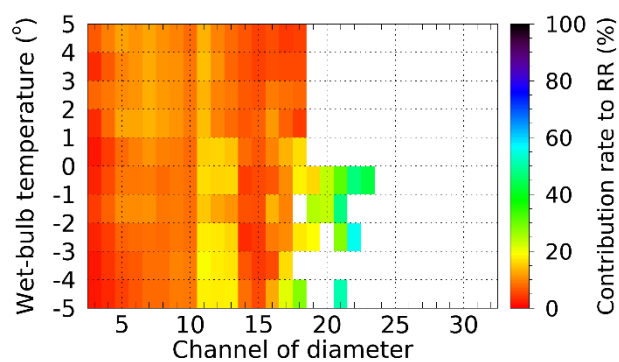
(c) Method 2



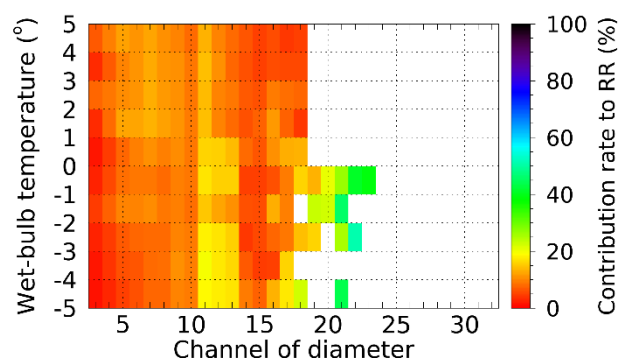
(d) Method 2 (melted)



(e) Method 3



(f) Method 3 (melted)



480 **Figure 14: Precipitation contribution rate by diameter channel for  $T_w$  using the pre-processing method based on falling velocity.**



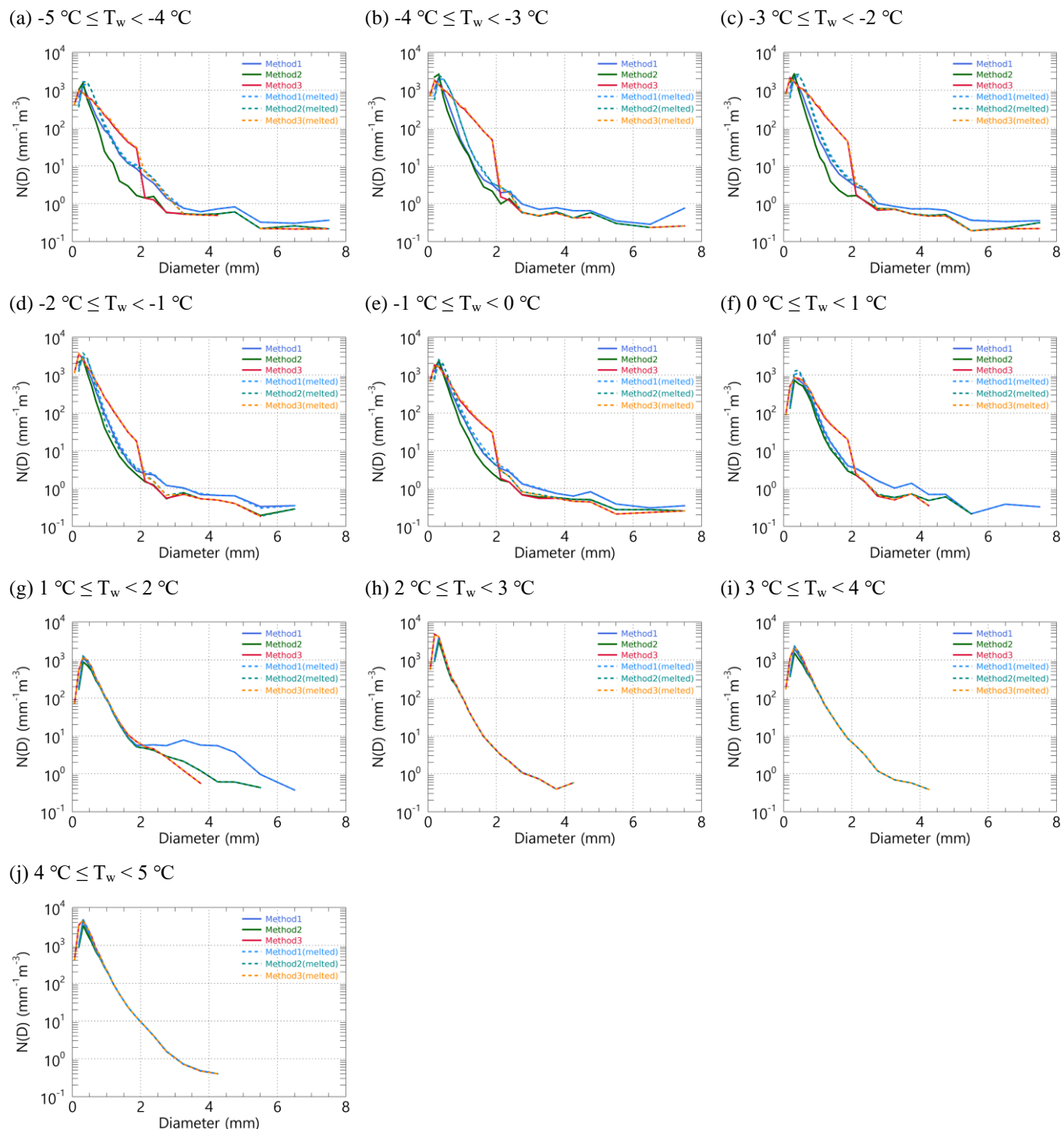
## 4.6 Drop size distribution

### 4.6.1 Number concentration calculated by applying QC methods based on $T_w$

The precipitation intensity derived from disdrometer data is contingent on the number concentration; therefore, examining the distribution of the number concentration is imperative. Figure 15 shows the average distribution of the number concentration obtained by applying the QC method under varying  $T_w$  conditions. Notably, when the temperature exceeded 2 °C, the distributions yielded by all QC methods were comparable. Method 3 exhibited a relatively high concentration of small droplets measuring 1 mm or less, whereas the number of droplets measuring 1 mm or more showed minimal variation (Fig. 15h). This finding indicates that, at temperatures above 2 °C, the output values remain consistent across different QC methods.

At temperatures ranging from 1 to 2 °C, the distribution of particles exceeding 2 mm in size was distinctly differentiated according to the QC method employed. This finding suggests that the fall velocity of particles larger than 2 mm exhibits considerable variation within this temperature interval (Fig. 10). Conversely, at temperatures below 1 °C, the distribution obtained through Method 3 displayed an anomalous pattern. This irregularity can be attributed to the failure of Method 3 to exclude snow particles smaller than 2 mm, leading to a higher concentration than that of the other QC methods. When considering the scenario in which particles are assumed to have melted, an increase in the concentration of water was observed for particles with a diameter of 1 mm or less when the  $T_w$  was between 0 and 1 °C, while the concentration of particles larger than 2 mm remained relatively unchanged.

In comparing scenarios where particles are assumed to have melted versus those that are not, no notable differences were observed at temperatures exceeding 1 °C (see Fig. 15g). However, within the temperature range of 0 to 1 °C, there was an increase in the number of particles smaller than 1 mm. There was a similar distribution in the number of medium and larger particles (1 mm or more). As the  $T_w$  progressively decreased below 0 °C, the disparity in the number concentration of particles larger than 1 mm became more pronounced (Fig. 15(a-e)).



514 **Figure 15: Average number concentration distribution for  $T_w$  using pre-processing methods.**



#### 515 4.6.2 Difference in the number concentration based on the gamma model

516 The change in the shape of the number concentration within the observed data has implications for DSD model parameters.  
517 The notable discrepancy between the observed number concentration and that derived from the model parameters raises  
518 concerns regarding the reliability of the DSD model.

519 Figures 16 and 17 show the variance between the observed number concentration and that predicted using the gamma model.  
520 When all QC methods were implemented, the MAPE remained below 60% across all diameter ranges at temperatures  
521 exceeding 2 °C. However, as the  $T_w$  fell below 1 °C, the discrepancy for diameters greater than 0.6 mm (CH 7) escalated to  
522 over 70%. At 2 °C or higher temperatures, the gamma distribution overestimated the concentration of particles smaller than 1  
523 mm while underestimating those larger than 1 mm. Nonetheless, the extent of under- or over-simulation by gamma  
524 distribution remained below 50% across all diameter intervals.

525 When  $T_w$  was below 1 °C, assuming that the snow particles had melted, the error rate in simulating the concentration of  
526 particles smaller than 1 mm (CH 8) diminished (Fig. 16(b, d)). Concurrently, the percentage bias (PBAIS) for particle  
527 diameters less than 1 mm decreased, approaching a value near zero (Fig. 17(b, d)). This phenomenon can be attributed to the  
528 application of the QC method under subzero conditions, which led to an overestimation of the gamma distribution for  
529 diameters of 1 mm or less because of the increased influence of smaller particles resulting from the exclusion of larger  
530 particles exceeding 3 mm. Conversely, this resulted in an underestimation of the gamma distribution for diameters larger  
531 than 3 mm.

532

533

534

535

536

537

538

539

540

541

542

543

544

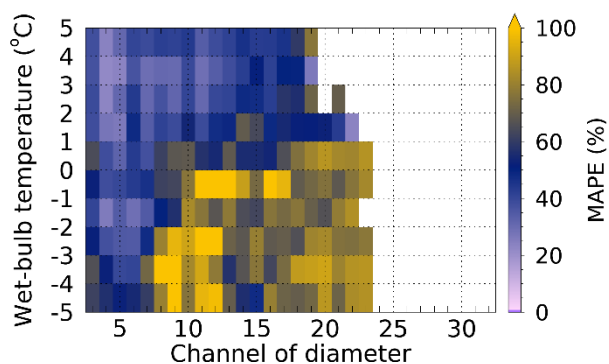
545

546

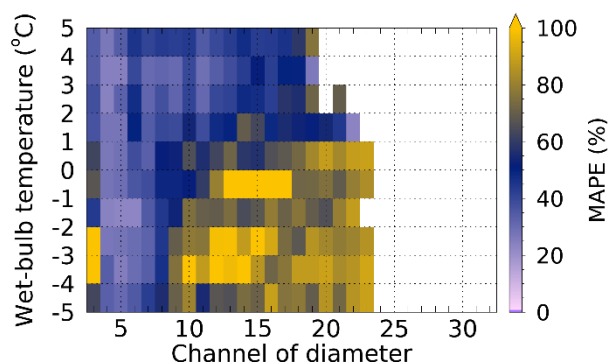
547



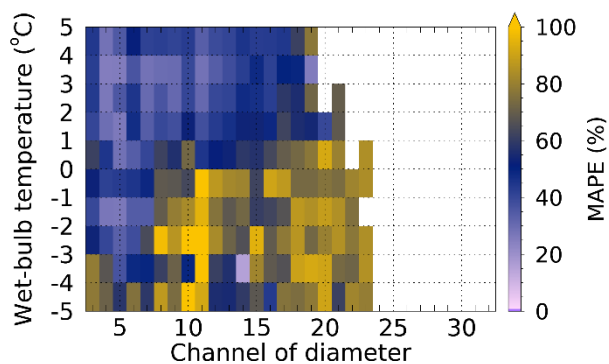
(a) Method 1



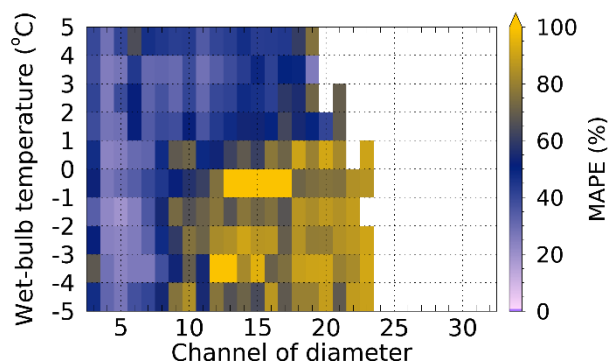
(b) Method 1 (melted)



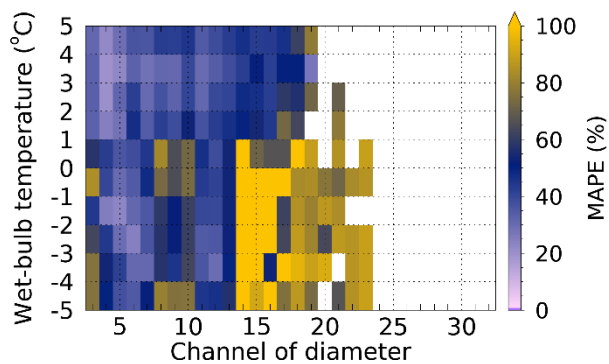
(c) Method 2



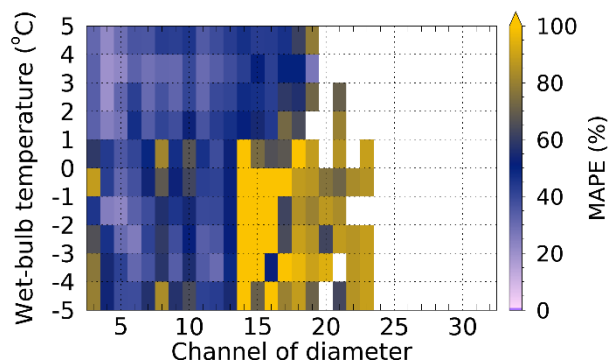
(d) Method 2 (melted)



(e) Method 3



(f) Method 3 (melted)



548 **Figure 16: MAPE for diameter and wet-bulb temperature using the pre-processing method**

549

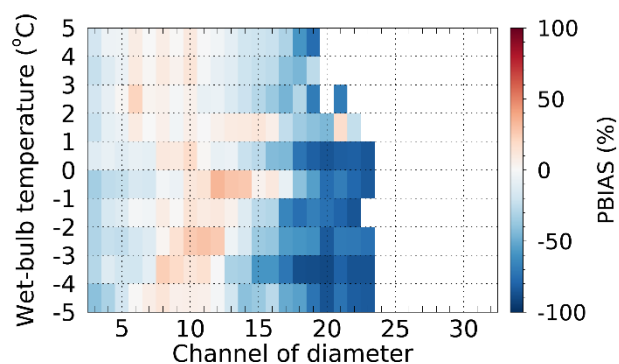
550

551

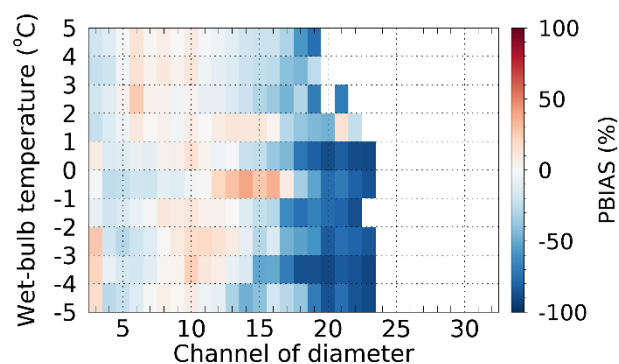
552



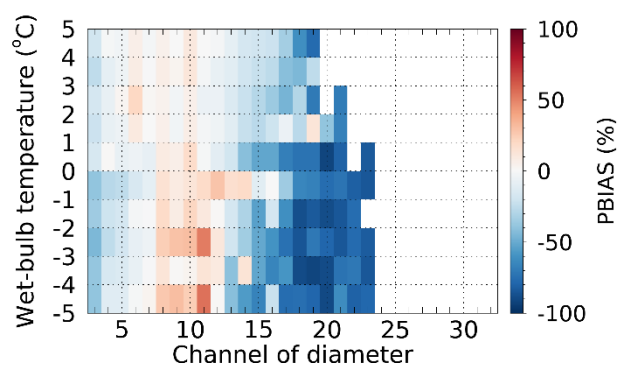
(a) Method 1



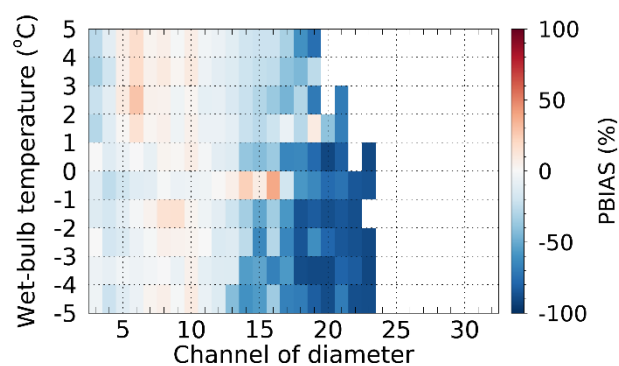
(b) Method 1 (melted)



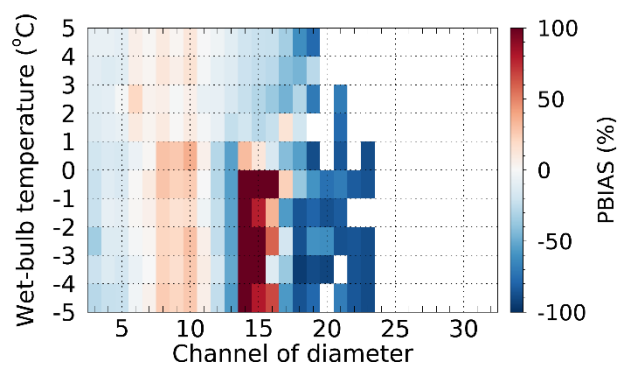
(c) Method 2



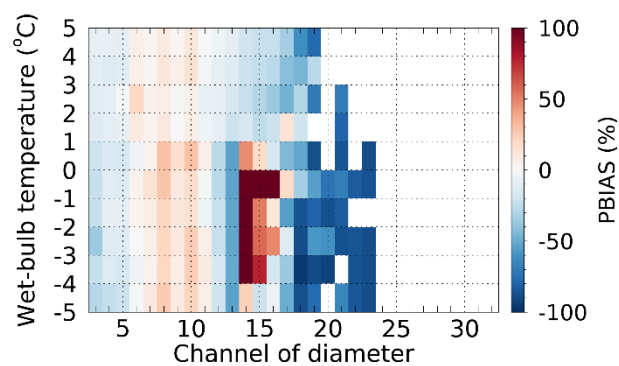
(d) Method 2 (melted)



(e) Method 3



(f) Method 3 (melted)



553 **Figure 17: PBAIS for diameter and wet-bulb temperature using the pre-processing method**

554



## 555 5 Conclusion

556 This study employed data collected from a 2DVD disdrometer in conjunction with traditional rain gauges to assess the  
557 precipitation measurements derived from the disdrometer under  $T_w$  conditions and to evaluate the reliability of the DSD  
558 model.

559 The precipitation estimates derived from the QC methods employed in this study exhibited  $CC \geq 0.98$  when juxtaposed with  
560 precipitation measurements obtained from rain gauges in an environment with  $T_w$  of 5 °C higher. The MAPE was  
561 approximately 8.5%. In contrast to scenarios in which the QC method was not implemented, the propensity for the 2DVD  
562 data to be overestimated diminished, and the overall error rate reduced. These findings indicate that all QC methods  
563 demonstrated high reliability under rainfall conditions.

564 When  $T_{air}$  and  $T_w$  dropped below 1 °C, there was a notable reduction in the fall velocity of precipitation particles, which  
565 became concentrated within a velocity range of approximately 0.5 to 3 m s<sup>-1</sup>. Moreover, the ratio of snow particles to  
566 raindrops considerably increased at temperatures below 1 °C for  $T_{air}$  and  $T_w$ . This observation is consistent with the findings  
567 of Ding et al. (2014), which indicated that the proportion of rain was less than 30% at temperatures below this threshold.  
568 Conversely, when  $T_{air}$  ranged from 1 to 3 °C, the distribution of fall velocities exhibited a broader range compared to  
569 conditions where  $T_w$  was between 1 and 3 °C, resulting in a greater disparity with the terminal velocity of raindrops.  
570 Consequently, it is justifiable to use  $T_w$  as a reference parameter to differentiate between types of precipitation using  
571 disdrometer data.

572 The fall velocity of particles exceeding 2 mm in diameter decreased within the 1 to 2 °C temperature range for  $T_w$ .  
573 Conversely, at  $T_w$  below 1 °C, the observed results were outside the effective fall velocity range typically associated with  
574 raindrops. Furthermore, as  $T_w$  decreased below 2 °C, the quantitative error, as measured by the correlation of disdrometer-  
575 based precipitation data, increased. These results can be attributed to the fact that the filter ratio for particles measuring 3  
576 mm or less escalated to 30% or higher when  $T_w$  was below 2 °C. Within this  $T_w$  range, it is plausible to regard raindrops and  
577 solid particles as intermixed; consequently, implementing QC methods appropriate for conventional rainfall scenarios may  
578 lead to inaccuracies. However, when snow particles were assumed to have undergone melting, the correlation approached  
579 0.9, even within the temperature range of 0 to 1 °C, and the variability of the error decreased. These findings indicate that the  
580 reliability of precipitation calculations can be maintained, even in scenarios where raindrops and snow particles coexist at  
581 temperatures between 0 and 2 °C, provided that an appropriate density for snow particles is used. Additionally, it is  
582 recommended that a weighing rain gauge be employed to verify precipitation when  $T_w$  is below 2 °C.

583 At 2 °C or higher  $T_w$ , the DSD shape remained consistent across different QC methods. However, as the temperature dropped  
584 below 2 °C, Method 1, which defines the raindrop size interval as  $\pm 40\%$  of the terminal velocity, indicated a comparatively  
585 elevated number of drops measuring 2 mm or larger. In conditions where the temperature was below 1 °C, the application of  
586 Method 3 (Raupach et al., 2015) resulted in a notable and irregular distribution of number concentration for droplet  
587 diameters ranging from 1 to 2 mm. These findings can be attributed to the QC method employed, which raises concerns





588 about the reliability of the DSD parameters derived from the altered shape of the DSD. Consequently, it is imperative to use  
589 disdrometer data corresponding to environmental conditions with temperatures of 2 °C or higher when calculating DSD  
590 parameters and DSD-based rain rates.

## 591 **Appendices**

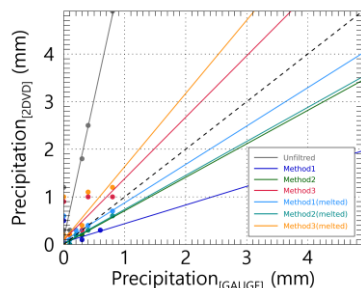
592 Figures A1 and A2 present the findings from a comparative analysis of hourly accumulated precipitation intensity, derived  
593 from observations using the 2DVD and two types of rain gauges (A1 represents the tipping-bucket type and A2 represents  
594 the weighing type) under the specified  $T_w$  interval conditions at 1 °C intervals. In each figure, the solid line denotes the  
595 regression line correlating the precipitation intensities derived by applying each quality control (QC) method. The constants  
596 and validation indices associated with the regression lines are listed in Tables A1 and A2, respectively. Tables A3 and A4  
597 provide details regarding the diameter and velocity channels used to calculate the number concentration based on 2DVD data.  
598 The channel information corresponded to the values employed in the PARSIVEL disdrometer data.

599  
600  
601  
602  
603  
604  
605  
606  
607  
608  
609  
610  
611  
612  
613  
614  
615  
616  
617  
618  
619

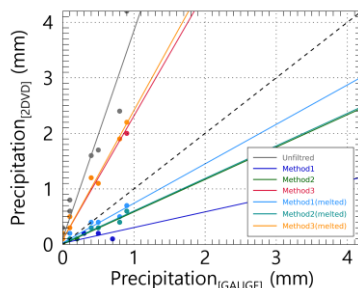


620

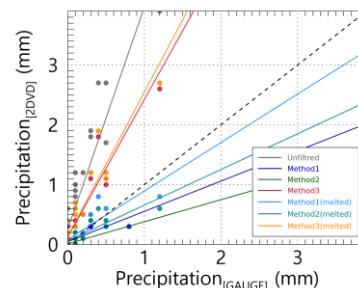
(a)  $-5^{\circ}\text{C} \leq T_w < -4^{\circ}\text{C}$



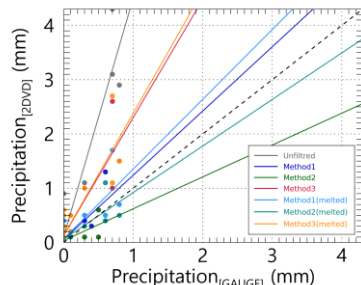
(b)  $-4^{\circ}\text{C} \leq T_w < -3^{\circ}\text{C}$



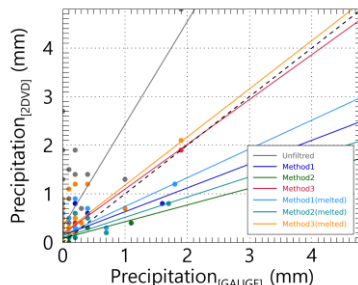
(c)  $-3^{\circ}\text{C} \leq T_w < -2^{\circ}\text{C}$



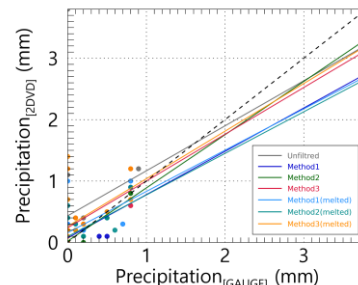
(d)  $-2^{\circ}\text{C} \leq T_w < -1^{\circ}\text{C}$



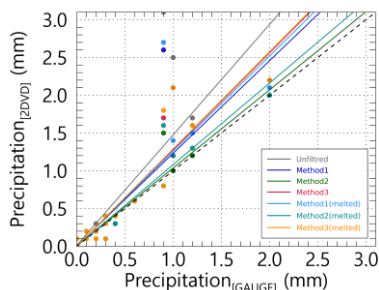
(e)  $-1^{\circ}\text{C} \leq T_w < 0^{\circ}\text{C}$



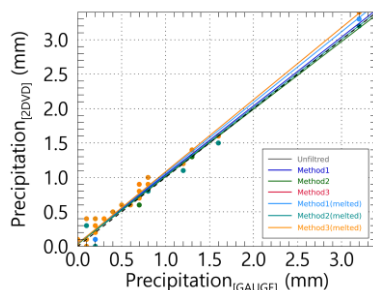
(f)  $0^{\circ}\text{C} \leq T_w < 1^{\circ}\text{C}$



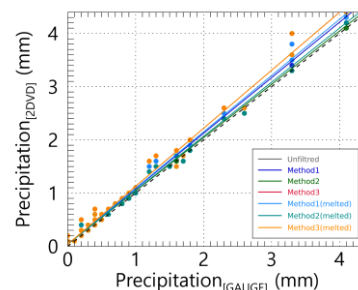
(g)  $1^{\circ}\text{C} \leq T_w < 2^{\circ}\text{C}$



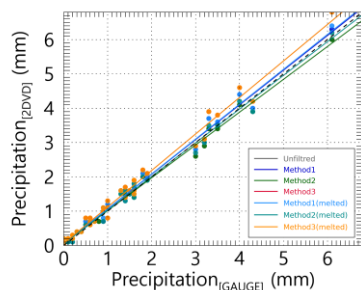
(h)  $2^{\circ}\text{C} \leq T_w < 3^{\circ}\text{C}$



(i)  $3^{\circ}\text{C} \leq T_w < 4^{\circ}\text{C}$



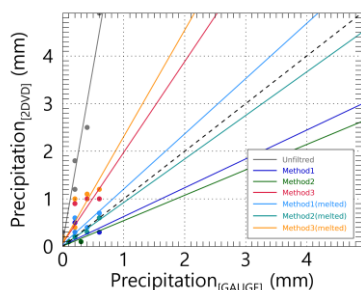
(j)  $4^{\circ}\text{C} \leq T_w < 5^{\circ}\text{C}$



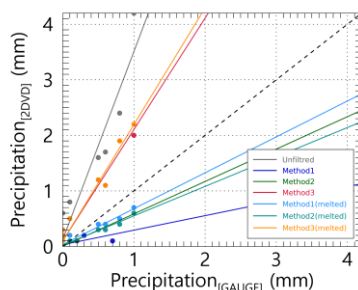


621 **Figure A1: Precipitation intensity scatter plot based on tipping-bucket rain gauge and 2DVD observation data for each  $T_w$  range.**  
622 **Each color in the scatter plot represents a filtering method.**

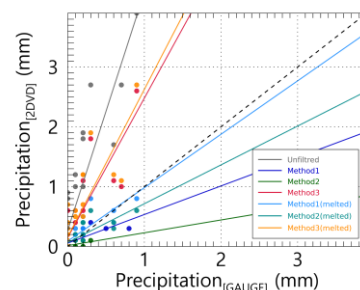
(a)  $-5\text{ }^{\circ}\text{C} \leq T_w < -4\text{ }^{\circ}\text{C}$



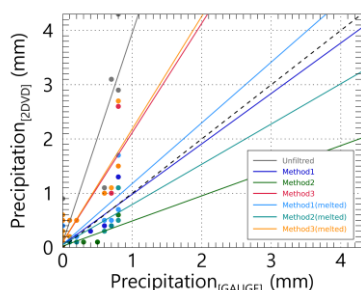
(b)  $-4\text{ }^{\circ}\text{C} \leq T_w < -3\text{ }^{\circ}\text{C}$



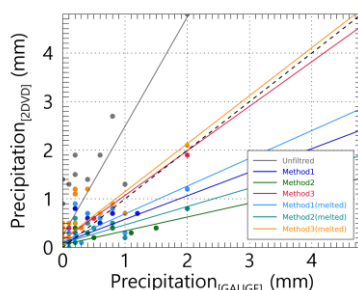
(c)  $-3\text{ }^{\circ}\text{C} \leq T_w < -2\text{ }^{\circ}\text{C}$



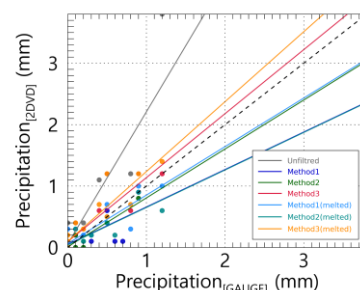
(d)  $-2\text{ }^{\circ}\text{C} \leq T_w < -1\text{ }^{\circ}\text{C}$



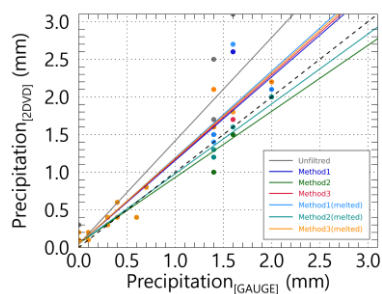
(e)  $-1\text{ }^{\circ}\text{C} \leq T_w < 0\text{ }^{\circ}\text{C}$



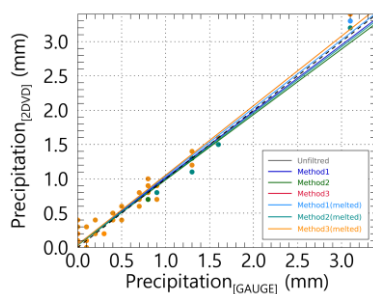
(f)  $0\text{ }^{\circ}\text{C} \leq T_w < 1\text{ }^{\circ}\text{C}$



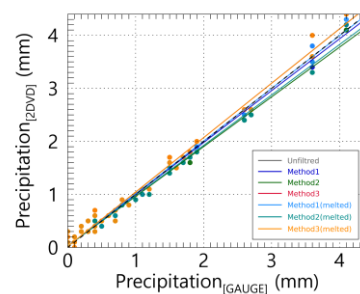
(g)  $1\text{ }^{\circ}\text{C} \leq T_w < 2\text{ }^{\circ}\text{C}$



(h)  $2\text{ }^{\circ}\text{C} \leq T_w < 3\text{ }^{\circ}\text{C}$



(i)  $3\text{ }^{\circ}\text{C} \leq T_w < 4\text{ }^{\circ}\text{C}$



(j)  $4\text{ }^{\circ}\text{C} \leq T_w < 5\text{ }^{\circ}\text{C}$

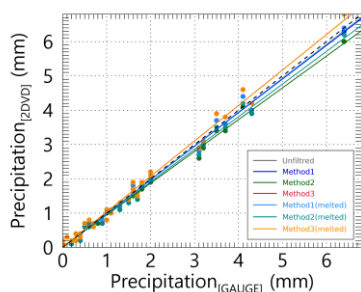




Figure A2: Precipitation intensity scatter plot based on weighing rain gauge and 2DVD observation data for each  $T_w$  range. Each color in the scatter plot represents a filtering method.

Table A1: Comparison of precipitation intensity based on tipping-bucket rain gauge and 2DVD observation data for each  $T_w$  range.

		T1	T2	T3	T4	T5	T6	T7	T8	T9	T10
Unfiltered	$a_1$	5.88	3.74	3.72	4.40	2.11	0.73	1.46	1.05	1.09	1.06
	$a_0$	0.12	0.11	0.25	0.11	0.32	0.43	0.01	0.04	0.04	0.06
	RMSE	1.01	0.91	0.92	0.96	0.85	0.92	0.46	0.10	0.17	0.23
	MAE	0.44	0.47	0.56	0.45	0.45	0.40	0.16	0.06	0.10	0.16
	MAPE	48.71	55.32	60.15	50.58	50.86	43.25	34.45	15.68	13.54	21.14
	CC	0.97	0.97	0.93	0.95	0.74	0.23	0.85	0.99	0.99	0.99
Method 1	$a_1$	0.39	0.28	0.51	1.18	0.49	0.71	1.23	1.00	1.04	1.01
	$a_0$	0.04	0.02	0.05	0.06	0.14	0.07	0.01	0.04	0.04	0.05
	RMSE	0.17	0.18	0.12	0.21	0.29	0.20	0.30	0.09	0.12	0.16
	MAE	0.08	0.07	0.05	0.11	0.15	0.11	0.10	0.06	0.07	0.12
	MAPE	28.57	56.67	27.24	34.01	37.07	56.39	31.27	17.96	12.04	16.83
	CC	0.45	0.75	0.78	0.79	0.55	0.66	0.89	0.99	1.00	0.99
Method 2	$a_1$	0.70	0.58	0.37	0.59	0.34	0.87	1.03	0.98	1.00	0.96
	$a_0$	0.01	0.00	0.01	0.03	0.08	0.02	0.00	0.03	0.04	0.06
	RMSE	0.03	0.03	0.06	0.13	0.20	0.09	0.12	0.08	0.08	0.13
	MAE	0.01	0.01	0.04	0.07	0.10	0.06	0.05	0.05	0.05	0.09
	MAPE	5.56	11.11	23.81	57.78	41.67	26.56	26.79	12.78	10.54	13.44
	CC	0.98	0.94	0.60	0.67	0.57	0.91	0.97	0.99	1.00	1.00
Method 3	$a_1$	1.29	2.22	2.30	2.18	0.92	0.76	1.28	1.05	1.09	1.06
	$a_0$	0.09	0.09	0.12	0.13	0.18	0.24	0.00	0.04	0.04	0.06
	RMSE	0.24	0.44	0.47	0.49	0.33	0.43	0.25	0.10	0.17	0.23
	MAE	0.11	0.26	0.28	0.26	0.18	0.23	0.10	0.06	0.10	0.16
	MAPE	38.75	49.04	51.11	47.07	45.58	46.25	25.58	15.68	13.54	21.14
	CC	0.76	0.99	0.94	0.87	0.73	0.47	0.94	0.99	0.99	0.99
Method 1 (melted)	$a_1$	0.81	0.71	0.81	1.29	0.59	0.67	1.26	1.03	1.06	1.02
	$a_0$	0.07	0.03	0.08	0.07	0.15	0.16	0.01	0.04	0.03	0.05
	RMSE	0.16	0.10	0.15	0.25	0.28	0.31	0.32	0.09	0.13	0.16
	MAE	0.06	0.05	0.09	0.12	0.16	0.16	0.11	0.06	0.08	0.12
	MAPE	26.33	21.39	34.06	31.87	42.73	38.50	31.64	18.03	12.37	16.51
	CC	0.76	0.97	0.85	0.82	0.66	0.51	0.88	0.99	1.00	0.99



Method 2 (melted)	$a_1$	0.71	0.59	0.60	0.86	0.42	0.68	1.08	0.99	1.02	0.98
	$a_0$	0.02	0.02	0.06	0.06	0.10	0.10	0.00	0.03	0.04	0.05
	RMSE	0.09	0.14	0.15	0.17	0.25	0.21	0.14	0.08	0.09	0.13
	MAE	0.05	0.07	0.08	0.09	0.13	0.12	0.06	0.05	0.05	0.10
	MAPE	17.78	23.33	27.88	31.87	45.37	44.88	27.62	12.84	11.00	15.80
	CC	0.93	0.98	0.84	0.79	0.67	0.65	0.96	0.99	1.00	1.00
Method 3 (melted)	$a_1$	1.54	2.33	2.41	2.25	0.99	0.77	1.29	1.05	1.09	1.06
	$a_0$	0.10	0.08	0.14	0.13	0.19	0.26	0.00	0.04	0.04	0.06
	RMSE	0.27	0.46	0.51	0.51	0.35	0.46	0.26	0.10	0.17	0.23
	MAE	0.13	0.27	0.30	0.28	0.20	0.25	0.11	0.06	0.10	0.16
	MAPE	40.50	49.24	50.27	47.38	46.46	45.30	28.44	15.68	13.54	21.14
	CC	0.79	0.99	0.93	0.87	0.74	0.45	0.93	0.99	0.99	0.99

626

627 **Table A2: Comparison of precipitation intensity based on weighing rain gauge and 2DVD observation data for each  $T_w$  range.**

		T1	T2	T3	T4	T5	T6	T7	T8	T9	T10
Unfiltered	$a_1$	7.36	3.39	3.98	3.86	2.25	2.15	1.37	1.01	1.03	1.03
	$a_0$	0.09	0.12	0.27	0.09	0.24	0.06	0.04	0.04	0.02	0.01
	RMSE	1.04	0.88	0.95	0.93	0.76	0.64	0.33	0.14	0.12	0.17
	MAE	0.44	0.46	0.57	0.43	0.43	0.31	0.15	0.08	0.07	0.12
	MAPE	49.76	55.42	60.80	48.81	53.44	41.61	41.39	22.03	13.07	19.05
	CC	0.98	0.97	0.90	0.93	0.88	0.89	0.95	0.98	0.99	0.99
Method 1	$a_1$	0.61	0.26	0.48	0.93	0.48	0.61	1.11	0.97	0.98	0.98
	$a_0$	0.02	0.03	0.06	0.05	0.09	0.05	0.04	0.05	0.02	0.01
	RMSE	0.13	0.17	0.13	0.19	0.28	0.20	0.20	0.13	0.10	0.14
	MAE	0.06	0.07	0.07	0.12	0.13	0.11	0.10	0.08	0.07	0.10
	MAPE	25.71	63.33	41.35	41.49	36.12	79.17	38.21	22.17	14.21	21.89
	CC	0.70	0.65	0.73	0.80	0.79	0.71	0.96	0.98	0.99	1.00
Method 2	$a_1$	0.53	0.58	0.21	0.46	0.28	0.80	0.88	0.95	0.94	0.93
	$a_0$	0.01	0.00	0.01	0.03	0.06	0.01	0.05	0.03	0.03	0.02
	RMSE	0.07	0.03	0.09	0.18	0.31	0.10	0.11	0.12	0.11	0.17
	MAE	0.02	0.01	0.06	0.11	0.15	0.07	0.07	0.07	0.07	0.12
	MAPE	22.22	11.11	28.57	85.56	55.43	27.34	35.56	18.32	14.12	20.69
	CC	0.82	0.94	0.45	0.75	0.78	0.92	0.98	0.98	1.00	1.00
Method 3	$a_1$	1.91	2.01	2.33	2.02	0.92	1.04	1.12	1.01	1.03	1.03



	$a_0$	0.07	0.10	0.15	0.10	0.15	0.10	0.05	0.04	0.02	0.01
	RMSE	0.22	0.41	0.52	0.45	0.29	0.21	0.16	0.14	0.12	0.17
	MAE	0.12	0.25	0.29	0.24	0.16	0.13	0.09	0.08	0.07	0.12
	MAPE	42.13	49.58	52.32	44.83	46.50	37.92	34.21	22.03	13.07	19.05
	CC	0.91	0.98	0.86	0.90	0.80	0.90	0.98	0.98	0.99	0.99
Method 1 (melted)	$a_I$	1.16	0.65	0.89	1.12	0.57	0.79	1.15	0.99	0.99	0.98
	$a_0$	0.05	0.03	0.09	0.06	0.12	0.06	0.04	0.04	0.02	0.01
	RMSE	0.11	0.13	0.16	0.23	0.26	0.16	0.21	0.13	0.10	0.13
	MAE	0.06	0.08	0.10	0.11	0.15	0.10	0.09	0.08	0.06	0.10
	MAPE	30.25	31.05	36.50	29.44	49.92	32.10	37.80	22.22	13.91	21.50
	CC	0.90	0.97	0.82	0.82	0.77	0.89	0.96	0.98	1.00	1.00
Method 2 (melted)	$a_I$	0.91	0.53	0.65	0.74	0.38	0.61	0.93	0.96	0.95	0.95
	$a_0$	0.01	0.02	0.07	0.05	0.09	0.04	0.05	0.04	0.02	0.01
	RMSE	0.04	0.18	0.14	0.17	0.29	0.18	0.09	0.12	0.11	0.15
	MAE	0.01	0.10	0.09	0.11	0.14	0.10	0.06	0.07	0.07	0.11
	MAPE	8.89	35.56	34.62	42.75	58.79	40.35	34.42	17.78	14.24	22.16
	CC	0.98	0.98	0.79	0.82	0.77	0.87	0.99	0.98	1.00	1.00
Method 3 (melted)	$a_I$	2.24	2.10	2.47	2.08	0.99	1.14	1.13	1.01	1.03	1.03
	$a_0$	0.07	0.10	0.16	0.11	0.16	0.10	0.05	0.04	0.02	0.01
	RMSE	0.27	0.44	0.55	0.48	0.30	0.22	0.16	0.14	0.12	0.17
	MAE	0.14	0.26	0.32	0.25	0.17	0.14	0.09	0.08	0.07	0.12
	MAPE	43.48	49.81	51.47	45.14	46.83	38.15	37.14	22.03	13.07	19.05
	CC	0.93	0.98	0.86	0.89	0.82	0.92	0.98	0.98	0.99	0.99

628  
629  
630  
631  
632  
633  
634  
635  
636  
637  
638



639 **Table A3: Diameter channel information of the PARSIVEL disdrometer.**

Channel number	Mid-value of channel (mm)	Diameter spread (mm)		Channel number	Mid-value of channel (mm)	Diameter spread (mm)
1	0.062	0.125		17	3.250	0.500
2	0.187	0.125		18	3.750	0.500
3	0.312	0.125		19	4.250	0.500
4	0.437	0.125		20	4.750	0.500
5	0.562	0.125		21	5.500	1.000
6	0.687	0.125		22	6.500	1.000
7	0.812	0.125		23	7.500	1.000
8	0.937	0.125		24	8.500	1.000
9	1.062	0.125		25	9.500	1.000
10	1.187	0.125		26	11.000	2.000
11	1.375	0.250		27	13.000	2.000
12	1.625	0.250		28	15.000	2.000
13	1.875	0.250		29	17.000	2.000
14	2.125	0.250		30	19.000	2.000
15	2.375	0.250		31	21.500	3.000
16	2.750	0.500		32	24.500	3.000

640

641

642

643

644

645

646

647

648

649

650

651





**Table A4: Velocity channel information of the PARSIVEL disdrometer.**

Channel number	Mid-value of channel (mm)	Velocity spread (mm)	Channel number	Mid-value of channel (mm)	Velocity spread (mm)
1	0.050	0.100	17	2.600	0.400
2	0.150	0.100	18	3.000	0.400
3	0.250	0.100	19	3.400	0.400
4	0.350	0.100	20	3.800	0.400
5	0.450	0.100	21	4.400	0.800
6	0.550	0.100	22	5.200	0.800
7	0.650	0.100	23	6.000	0.800
8	0.750	0.100	24	6.800	0.800
9	0.850	0.100	25	7.600	0.800
10	0.950	0.100	26	8.800	1.600
11	1.100	0.200	27	10.400	1.600
12	1.300	0.200	28	12.000	1.600
13	1.500	0.200	29	13.600	1.600
14	1.700	0.200	30	15.200	1.600
15	1.900	0.200	31	17.600	3.200
16	2.200	0.400	32	20.800	3.200

653

654

#### 655 **Author contributions**

656 HJK and CJ, conceptualized the project. JB did the data curation and formal analysis. HJK and SHS did the analysis and  
657 interpretation. HJK and JB led the investigation. HJK prepared the original draft, and SHS and CJ reviewed and edited the  
658 paper. All authors have read and agreed to the published version of the paper.

#### 659 **Acknowledgements**

660 This study was supported by the Basic Science Research Program through the National Research Foundation of Korea  
661 (NRF), funded by the Ministry of Education (RS-2022-NR071182).

662

#### 663 **Competing Interest**

664 The contact author has declared that none of the authors has any competing interests.



## References

- Atlas, D., Srivastava, R. C., and Sekhon, R. S.: Doppler radar characteristics of precipitation at vertical incidence, *Rev. Geophys.*, 11, 1–35. <https://doi.org/10.1029/RG011i001p00001>, 1973.
- Barthazy, E. and Schefold, R.: Fall velocity of snowflakes of different riming degree and crystal types, *Atmos. Res.*, 82, 391–398. <https://doi.org/10.1016/j.atmosres.2005.12.009>, 2006.
- Beard, K. V.: Terminal velocity adjustment for cloud and precipitation drops aloft, *J. Atmos. Sci.*, 34, 1293–1298. [https://doi.org/10.1175/1520-0469\(1977\)034<1293:TVAFCA>2.0.CO;2](https://doi.org/10.1175/1520-0469(1977)034<1293:TVAFCA>2.0.CO;2), 1977.
- Brandes, E. A., Zhang, G., and Vivekanandan, J.: Experiments in rainfall estimation with a polarimetric radar in a subtropical environment, *J. Appl. Meteor.*, 41, 674–685. [https://doi.org/10.1175/1520-0450\(2002\)041<0674:EIREWA>2.0.CO;2](https://doi.org/10.1175/1520-0450(2002)041<0674:EIREWA>2.0.CO;2), 2002.
- Chang, W. Y., Wang, T. C. C., and Lin, P. L.: Characteristics of the raindrop size distribution and drop shape relation in typhoon systems in the western Pacific from the 2D video disdrometer and NCU C-band polarimetric radar, *J. Atmos. Ocean. Technol.*, 26, 1973–1993. <https://doi.org/10.1175/2009JTECHA1236.1>, 2009.
- Dahlström, B.: Cloud physical and climatological factors for the determination of rain intensity, *Water*, 13, 2292. <https://doi.org/10.3390/w13162292>, 2021.
- Delanoë, J., Protat, A., Testud, J., Bouniol, D., Heymsfield, A. J., Bansemer, A., Brown, P. R. A., Forbes, R. M.: Statistical properties of the normalized ice particle size distribution, *J. Geophys. Res. Atmos.*, 110. <https://doi.org/10.1029/2004JD005405>, 2005.
- Deo, A. and Walsh, K. J. E.: Contrasting tropical cyclone and non-tropical cyclone related rainfall drop size distribution at Darwin, Australia, *Atmos. Res.*, 181, 81–94. <https://doi.org/10.1016/j.atmosres.2016.06.015>, 2016.
- Ding, B., Yang, K., Qin, J., Wang, L., Chen, Y., and He, X.: The dependence of precipitation types on surface elevation and meteorological conditions and its parameterization, *J. Hydrol.*, 513, 154–163. <https://doi.org/10.1016/j.jhydrol.2014.03.038>, 2014.
- Du, Y. and Chen, G.: Heavy rainfall associated with double low-level jets over southern China. Part II: Convection initiation, *Mon. Weather Rev.*, 147, 543–565. <https://doi.org/10.1175/MWR-D-18-0102.1>, 2019.
- Friedrich, K., Kalina, E. A., Masters, F. J., and Lopez, C. R.: Drop-size distributions in thunderstorms measured by optical disdrometers during VORTEX2, *Mon. Weather Rev.*, 141, 1182–1203. <https://doi.org/10.1175/MWR-D-12-00116.1>, 2013.
- Gong, Y., He, T., Chen, M., Wang, B., Nie, L., and Yin, Y.: Spatio-temporal enhanced contrastive and contextual learning for weather forecasting, *IEEE Trans. Knowl. Data Eng.*, 36, 4260–4274. <https://doi.org/10.1109/TKDE.2024.3362825>, 2024.



- 696 Grazioli, J., Tuia, D., Monhart, S., Schneebeli, M., Raupach, T., and Berne, A.: Hydrometeor classification from two-  
697 dimensional video disdrometer data, *Atmos. Meas. Tech.*, 7, 2869–2882. <https://doi.org/10.5194/amt-7-2869-2014>,  
698 2014.
- 699 Guo, J., Liu, H., Li, Z., Rosenfeld, D., Jiang, M., Xu, W., Jiang, J. H., He, J., Chen, D., Min, M., Zhai, P.: Aerosol-induced  
700 changes in the vertical structure of precipitation: A perspective of TRMM precipitation radar, *Atmos. Chem. Phys.*, 18,  
701 13329–13343. <https://doi.org/10.5194/acp-18-13329-2018>, 2018.
- 702 Hu, A. Z. and Igel, A. L.: A bin and a bulk microphysics scheme can be more alike than two bin schemes, *J. Adv. Model.*  
703 *Earth Syst.*, 15, MS003303, e2022. <https://doi.org/10.1029/2022MS003303>, 2023.
- 704 Insel, N., Poulsen, C. J., and Ehlers, T. A.: Influence of the Andes Mountains on South American moisture transport,  
705 convection, and precipitation, *Clim. Dyn.*, 35, 1477–1492. <https://doi.org/10.1007/s00382-009-0637-1>, 2010.
- 706 Iversen, E. C., Thompson, G., and Nygaard, B. E.: Improvements to melting snow behavior in a bulk microphysics scheme,  
707 *Atmos. Res.*, 253, 105471. <https://doi.org/10.1016/j.atmosres.2021.105471>, 2021.
- 708 Jaffrain, J. and Berne, A.: Experimental quantification of the sampling uncertainty associated with measurements from  
709 PARSIVEL disdrometers, *J. Hydrol. Meteorol.*, 12, 352–370. <https://doi.org/10.1175/2010JHM1244.1>, 2011.
- 710 Ji, L., Chen, H., Li, L., Chen, B., Xiao, X., Chen, M., and Zhang, G.: Raindrop size distributions and rain characteristics  
711 observed by a PARSIVEL disdrometer in Beijing, Northern China, *Remote Sens.*, 11, 1479.  
712 <https://doi.org/10.3390/rs11121479>, 2019.
- 713 Kim, H. J., Jung, W., Suh, S. H., Lee, D. I., and You, C. H.: The characteristics of raindrop size distribution at windward and  
714 leeward side over mountain area, *Remote Sens.*, 14, 2419. <https://doi.org/10.3390/rs14102419>, 2022.
- 715 Kim, H. J., Lee, K. O., You, C. H., Uyeda, H., and Lee, D. I.: Microphysical characteristics of a convective precipitation  
716 system observed on July 04, 2012, over Mt. Halla in South Korea, *Atmos. Res.*, 222, 74–87.  
717 <https://doi.org/10.1016/j.atmosres.2019.02.011>, 2019.
- 718 Kochendorfer, J., Earle, M. E., Hodyss, D., Reverdin, A., Roulet, Y. A., Nitu, R., Rasmussen, R., Landolt, S., Buisán, S.,  
719 Laine, T.: Undercatch adjustments for tipping-bucket gauge measurements of solid precipitation, *J. Hydrol. Meteorol.*,  
720 21, 1193–1205. <https://doi.org/10.1175/JHM-D-19-0256.1>, 2020.
- 721 Kruger, A. and Krajewski, W. F.: Two-dimensional video disdrometer: A description, *J. Atmos. Ocean. Technol.*, 19, 602–  
722 617. [https://doi.org/10.1175/1520-0426\(2002\)019<0602:TDVDAD>2.0.CO;2](https://doi.org/10.1175/1520-0426(2002)019<0602:TDVDAD>2.0.CO;2), 2002.
- 723 Lee, K. O., Uyeda, H., and Lee, D. I.: Microphysical structures associated with enhancement of convective cells over Mt.  
724 Halla, Jeju Island, Korea on 6 July 2007, *Atmos. Res.*, 135–136, 76–90.  
725 <https://doi.org/10.1016/j.atmosres.2013.08.012>, 2014.
- 726 Lintner, B. R., Adams, D. K., Schiro, K. A., Stansfield, A. M., Amorim Rocha, A. A., and Neelin, J. D.: Relationships  
727 among climatological vertical moisture structure, column water vapor, and precipitation over the central Amazon in  
728 observations and CMIP5 models, *Geophys. Res. Lett.*, 44, 1981–1989. <https://doi.org/10.1002/2016GL071923>, 2017.



- 729 Liu, X., Li, H., Hu, S., Wan, Q., Xiao, H., Zheng, T., Li, M., Ye, L., Guo, Z., Wang, Y., Yan, Z.: A high-precision and fast  
730 solution method of gamma raindrop size distribution based on 0-moment and 3-moment in South China, *J. Appl.*  
731 *Meteorol. Climatol.*, 60, 1407–1421. <https://doi.org/10.1175/JAMC-D-21-0043.1>, 2021.
- 732 Lu, Y., Yu, Z., Albertson, J. D., Chen, H., Hu, L., Pendergrass, A., Chen, X., Li, Q.: Understanding the influence of urban  
733 form on the spatial pattern of precipitation, *Earths Future*, 12, EF003846, e2023.  
734 <https://doi.org/10.1029/2023EF003846>, 2024.
- 735 Mahes Kumar, R. S., Padmakumari, B., Konwar, M., Morwal, S. B., and Deshpande, C. G.: Characterization of hydrometeors  
736 and precipitation over the Indian monsoon region using aircraft measurements, *Atmos. Res.*, 205, 147–154.  
737 <https://doi.org/10.1016/j.atmosres.2018.02.012>, 2018.
- 738 Marshall, J. S. and Palmer, W. M. K.: The distribution of raindrops with size, *J. Atmos. Sci.*, 5, 165–166.  
739 [https://doi.org/10.1175/1520-0469\(1948\)005<0165:TDORWS.2.0.CO;2](https://doi.org/10.1175/1520-0469(1948)005<0165:TDORWS.2.0.CO;2), 1948.
- 740 Marzuki, M., Randeu, W. L., Schönhuber, M., Bringi, V. N., Kozu, T., and Shimomai, T.: Raindrop size distribution  
741 parameters of distrometer data with different bin sizes, *IEEE Trans. Geosci. Remote Sens.*, 48, 3075–3080.  
742 <https://doi.org/10.1109/TGRS.2010.2043955>, 2010.
- 743 Padullés, R., Kuo, Y. H., Neelin, J. D., Turk, F. J., Ao, C. O., and De la Torre Juárez, M.: Global tropical precipitation  
744 relationships to free-tropospheric water vapor using radio occultations, *J. Atmos. Sci.*, 79, 1585–1600.  
745 <https://doi.org/10.1175/JAS-D-21-0052.1>, 2022.
- 746 Raupach, T. H. and Berne, A.: Correction of raindrop size distributions measured by Parsivel disdrometers, using a two-  
747 dimensional video disdrometer as a reference, *Atmos. Meas. Tech.*, 8, 343–365. [https://doi.org/10.5194/amt-8-343-](https://doi.org/10.5194/amt-8-343-2015)  
748 [2015](https://doi.org/10.5194/amt-8-343-2015), 2015.
- 749 Savina, M., Schäppi, B., Molnar, P., Burlando, P., and Sevruck, B.: Comparison of a tipping-bucket and electronic weighing  
750 precipitation gage for snowfall, *Atmos. Res.*, 103, 45–51. <https://doi.org/10.1016/j.atmosres.2011.06.010>, 2012.
- 751 Segovia-Cardozo, D. A., Rodríguez-Sinobas, L., Díez-Herrero, A., Zubelzu, S., and Canales-Ide, F.: Understanding the  
752 mechanical biases of tipping-bucket rain gauges: A semi-analytical calibration approach, *Water*, 13, 2285.  
753 <https://doi.org/10.3390/w13162285>, 2021.
- 754 Serio, M. A., Carollo, F. G., and Ferro, V.: Raindrop size distribution and terminal velocity for rainfall erosivity studies. A  
755 review, *J. Hydrol.*, 576, 210–228. <https://doi.org/10.1016/j.jhydrol.2019.06.040>, 2019.
- 756 Smith, P. L.: Raindrop size distributions: Exponential or gamma—Does the difference matter?, *J. Appl. Meteor.*, 42, 1031–  
757 1034. [https://doi.org/10.1175/1520-0450\(2003\)042<1031:RSDEOG>2.0.CO;2](https://doi.org/10.1175/1520-0450(2003)042<1031:RSDEOG>2.0.CO;2), 2003.
- 758 Steenburgh, W. J.: Sea-effect precipitation: A Look at Japan’s “Gosetsu Chitai”, *Bull. Am. Meteorol. Soc.*, 101, 129–136.  
759 <https://doi.org/10.1175/BAMS-D-18-0335.A>, 2020.
- 760 Stull, R.: Wet-bulb temperature from relative humidity and air temperature, *J. Appl. Meteorol. Climatol.*, 50, 2267–2269.  
761 <https://doi.org/10.1175/JAMC-D-11-0143.1>, 2011.



- 762 Syпка, P.: Dynamic real-time volumetric correction for tipping-bucket rain gauges, *Agric. Forest Meteorol.*, 271, 158–167.  
763 <https://doi.org/10.1016/j.agrformet.2019.02.044>, 2019.
- 764 Tang, Y. S., Chang, P. L., Chang, W. Y., Zhang, J., Tang, L., Lin, P. F., and Chen, C. R.: A localized quantitative  
765 precipitation estimation for S-band polarimetric radar in Taiwan, *J. Hydrol. Meteorol.*, 25, 1697–1712.  
766 <https://doi.org/10.1175/JHM-D-23-0205.1>, 2024.
- 767 Thomas, A., Kanawade, V. P., Chakravarty, K., and Srivastava, A. K.: Characterization of raindrop size distributions and its  
768 response to cloud microphysical properties, *Atmos. Res.*, 249, 105292.  
769 <https://doi.org/10.1016/j.atmosres.2020.105292>, 2021.
- 770 Thurai, M. and Bringi, V. N.: Drop axis ratios from a 2D video disdrometer, *J. Atmos. Ocean. Technol.*, 22, 966–978.  
771 <https://doi.org/10.1175/JTECH1767.1>, 2005.
- 772 Tiira, J., Moisseev, D. N., Von Lerber, A., Ori, D., Tokay, A., Bliven, L. F., and Petersen, W.: Ensemble mean density and  
773 its connection to other microphysical properties of falling snow as observed in Southern Finland, *Atmos. Meas. Tech.*,  
774 9, 4825–4841. <https://doi.org/10.5194/amt-9-4825-2016>, 2016.
- 775 Ulbrich, C. W.: Natural variations in the analytical form of the raindrop size distribution, *J. Clim. Appl. Meteorol.*, 22, 1764–  
776 1775. [https://doi.org/10.1175/1520-0450\(1983\)022<1764:NVITAF>2.0.CO;2](https://doi.org/10.1175/1520-0450(1983)022<1764:NVITAF>2.0.CO;2), 1983.
- 777 Vázquez-Martín, S., Kuhn, T., and Eliasson, S.: Mass of different snow crystal shapes derived from fall speed measurements,  
778 *Atmos. Chem. Phys.*, 21, 18669–18688. <https://doi.org/10.5194/acp-21-18669-2021>, 2021.
- 779 Wen, L., Zhao, K., Chen, G., Wang, M., Zhou, B., Huang, H., Hu, D., Lee, W. C., Hu, H.: Drop size distribution  
780 characteristics of seven typhoons in China, *J. Geophys. Res. Atmos.*, 123, 6529–6548.  
781 <https://doi.org/10.1029/2017JD027950>, 2018.
- 782 Yang, Q., Dai, Q., Han, D., Chen, Y., and Zhang, S.: Sensitivity analysis of raindrop size distribution parameterizations in  
783 WRF rainfall simulation, *Atmos. Res.*, 228, 1–13. <https://doi.org/10.1016/j.atmosres.2019.05.019>, 2019.
- 784 Yang, Y., Wang, R., Chen, F., Liu, C., Bi, X., and Huang, M.: Synoptic weather patterns modulate the frequency, type and  
785 vertical structure of summer precipitation over Eastern China: A perspective from GPM observations, *Atmos. Res.*, 249,  
786 105342. <https://doi.org/10.1016/j.atmosres.2020.105342>, 2021.
- 787 Yao, X., Yang, K., Zhou, X., Wang, Y., Lazhu, C., Chen, Y., and Lu, H.: Surface friction contrast between water body and  
788 land enhances precipitation downwind of a large lake in Tibet, *Clim. Dyn.*, 56, 2113–2126.  
789 <https://doi.org/10.1007/s00382-020-05575-x>, 2021.
- 790 Yi, Y., Yi, F., Liu, F., Zhang, Y., Yu, C., and He, Y.: Microphysical process of precipitating hydrometeors from warm-front  
791 mid-level stratiform clouds revealed by ground-based lidar observations, *Atmos. Chem. Phys.*, 21, 17649–17664.  
792 <https://doi.org/10.5194/acp-21-17649-2021>, 2021.
- 793